Shower Shapes and Data-Driven Simulation Studies using a Highly Granular Crystal ECAL [C01]

Jack Rolph, Yong Liu, Baohua Qi, Zhiyu Zhao
on behalf of the AGORA/CEPC Calorimetry Team

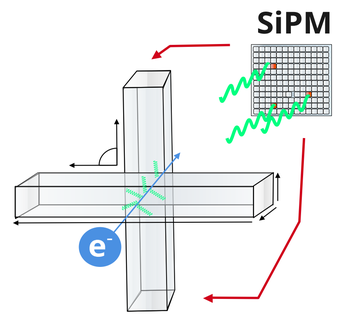
中国科学院高能物理研究所
Institute of High Energy Physics
Chinese Academy of Sciences

drdcalo

Overview

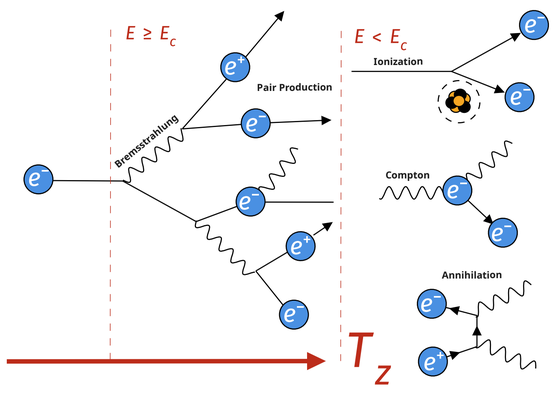
Highly Granular Crystal ECAL

- **criss-crossing scintillating crystal bars [1]:**
  - CEPC detector volume: 1.5 × 1.5 × 40 cm³
  - prototype volume: 2 × 2 × 12 cm³
  - homogeneous;
  - crystal: BGO/BSO;
- **granularity:**
  - particle separation capability
  - energy density information;
- **excellent EM energy resolution: stochastic term ~1-2%**



Shower Shapes

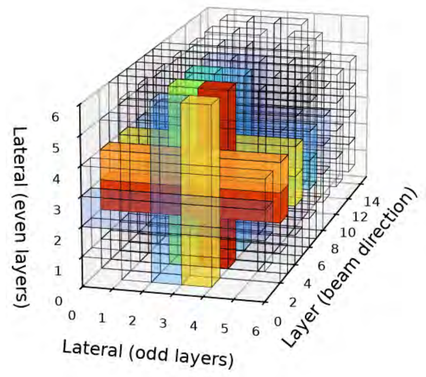
- **Shower shapes can be used for:**
  - studying shower fluctuations;
  - measuring absorber properties;
  - synthetic shower generation;
- **Gap in literature for shower shapes <1 GeV.**



Summary of Studies

2025 Testbeam Data

- Taken at Proton Synchrotron (PS) T9 Beamline;
- Electrons, 0.2-6 GeV
- ~2M electron events;
- PID used to select electrons;



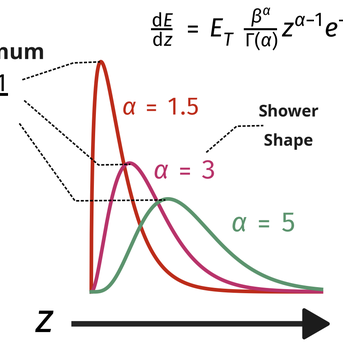
Fitted Shower Shape Models

- **Longitudinal Distribution: Gamma [2]**

$$\frac{dE}{dz} = E_T \frac{\beta^\alpha}{\Gamma(\alpha)} z^{\alpha-1} e^{-\beta z}$$

Shower Maximum

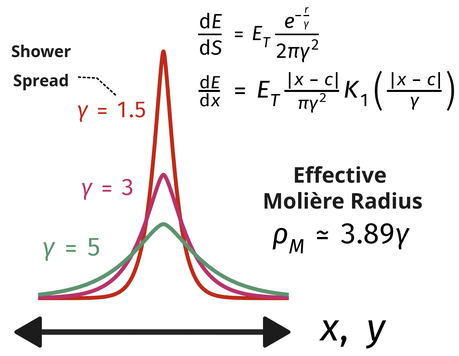
$$T_z = \frac{\alpha - 1}{\beta}$$



- **Lateral Distribution: Exponential/Bessel-K [3,4]**

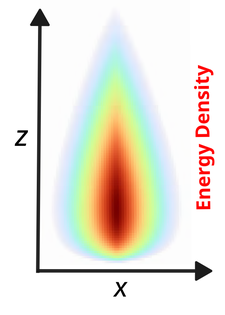
$$\frac{dE}{dS} = E_T \frac{e^{-\frac{r}{\gamma}}}{2\pi\gamma^2}$$

$$\frac{dE}{dx} = E_T \frac{|x-c|}{\pi\gamma^2} K_1\left(\frac{|x-c|}{\gamma}\right)$$



Effective Molière Radius

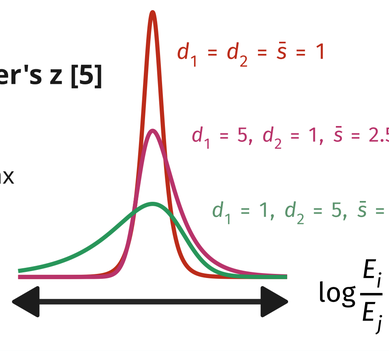
$$\rho_M \simeq 3.89\gamma$$



- **Log Energy Fraction Distribution: Fisher's z [5]**
(Difference of Log Gamma Variates)

Log ratios related to energy fractions by Softmax

$$[f_0, f_1 \cdots f_D] = \text{Softmax}\left(\left[\log\frac{E_0}{E_D}, \log\frac{E_1}{E_D}, \cdots \log\frac{E_{D-1}}{E_D}, 0\right]\right)$$

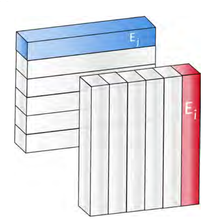


$$Y = \mu + \bar{s}\log R$$

$$R = \frac{X_1/d_1}{X_2/d_2}$$

$$X_1 \sim \chi^2_{d_1}$$

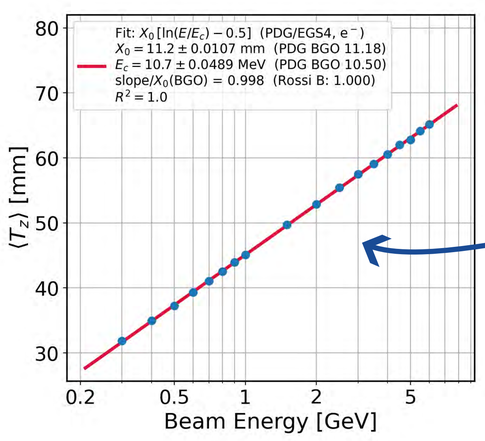
$$X_2 \sim \chi^2_{d_2}$$



Key Results

Physics Measurements of BGO and energy fractions

Mean T_z vs beam energy



Key Result:

$$\langle T_z \rangle = X_0\left(\log\left(\frac{E}{E_c}\right) - 0.5\right)$$

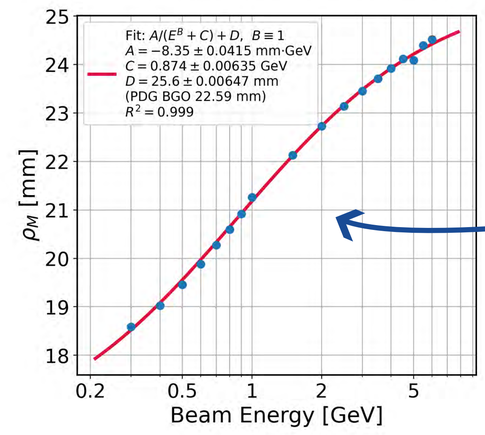
- **Radiation Length (X_0):**
  - Distance after which electron loses ~64% of its total energy;

PDG, BGO	Measurement
11.18 mm	11.2 ± 0.01 mm

- **Critical Energy (E_c):**
  - Below critical energy, EM shower extinction more probable than multiplication

PDG, BGO	Measurement
10.5 MeV	10.7 ± 0.05 MeV

Mean ρ_M vs beam energy



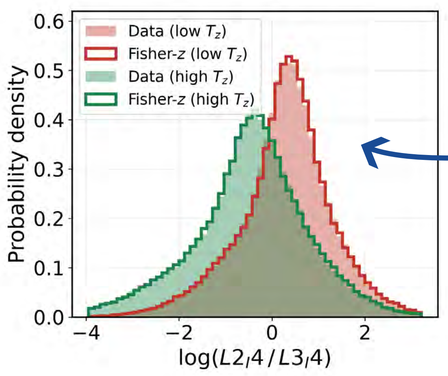
Key Result:

$$\langle \rho_M \rangle = \frac{A}{(E^B + C)} + D$$

- **Effective Molière Radius (D):**
  - Radius containing 90% of energy;
  - Larger than theory due to granularity/energy threshold

PDG, BGO	Measurement
22.59 mm	25.6 ± 0.06 mm

Log energy ratios conditioned on shower shape (electrons, E = 1 GeV)

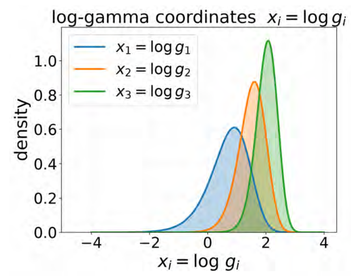


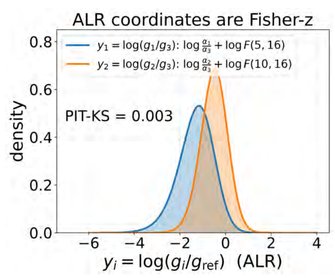
Key Result:

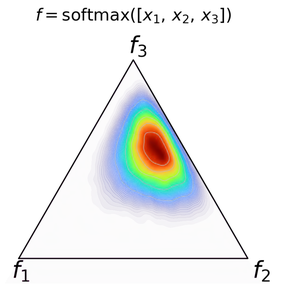
- Log fraction distribution fitted by Fisher's z distribution;
- Log fraction fully conditioned on shower shape
- Scale indicates correlation between cells;

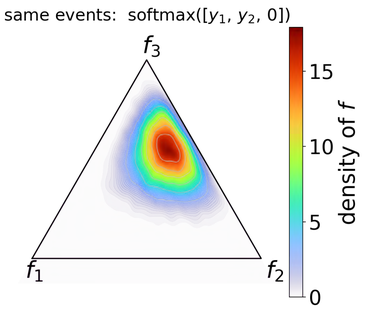
Generative Model using energy fraction distribution

- A fixed shower shape means log energy ratios drawn from Fisher's z distribution;
- Softmax maps log ratios to energy fractions;
- Equivalent to Softmax of zero-inflated log-Gamma variates;
- **Fast shower simulation method:**
  - *Generate correlated log-Gamma variates;*
  - *Apply Softmax operation;*
  - *Obtain energy fractions for each bar;*
- **Correlations from Gaussian Copula method;**
- **Fit of marginal/correlation matrix with censored log-likelihood for 'dark' bars;**

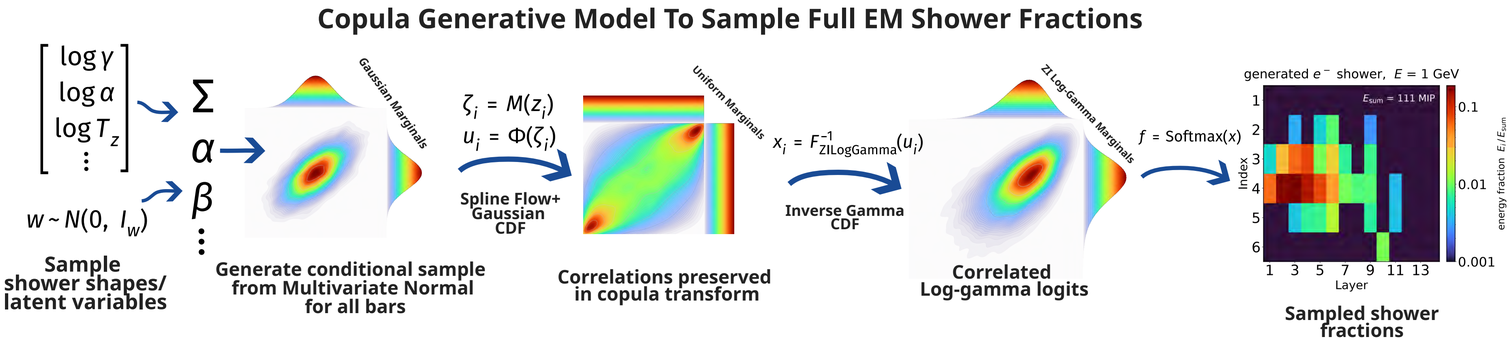




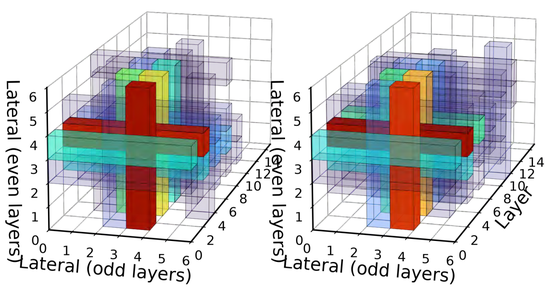


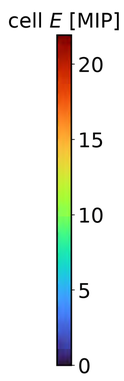


Copula Generative Model To Sample Full EM Shower Fractions



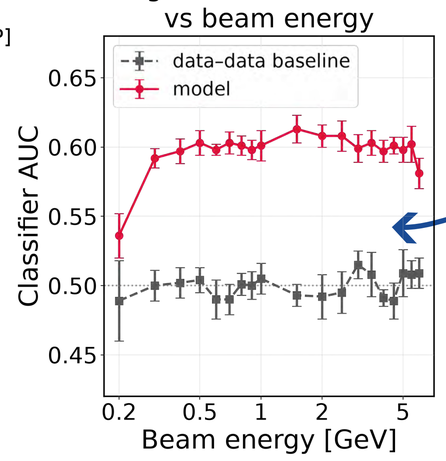
Data Model





E = 1 GeV, E_{sum} = 111 MIP

Data–generated classifier AUC vs beam energy



Key Result:

- DNN Classifier can only distinguish generated vs. real up to AUC=0.6;
- AUC within CaloChallenge 2022 review [6] top-5 range for electrons
- Global shower variables reconstructed with excellent agreement;
- Average generation time on GPU: 33 µs

[1] The CEPC Study Group, CEPC Technical Design Report -- Reference Detector, arXiv:2510.05260 [hep-ex] (2025), https://arxiv.org/abs/2510.05260.
[2] Grindhammer, G. & Peters, S., The Parameterized Simulation of Electromagnetic Showers in Homogeneous and Sampling Calorimeters, arXiv:hep-ex/0001020 (2000), DOI: 10.48550/arXiv.hep-ex/0001020
[3] O.L. Pinto, Shower Shapes in a Highly Granular SiPM-on-Tile Analog Hadron Calorimeter, PhD thesis, Universität Hamburg (2022), https://ediss.sub.uni-hamburg.de/handle/ediss/9855
[4] Bonamente, M., Properties and Approximations of a Bessel Distribution for Data Science Applications, Int. J. Stat. Distrib. Appl. 11(3) (2025) 85–97, DOI: 10.11648/j.ijsda.20251103.11
[5] Fisher, R.A., On a distribution yielding the error functions of several well known statistics, Proc. Int. Congr. Math., Toronto, vol. 2, pp. 805–813 (1924)
[6] Krause, C. et al., CaloChallenge 2022: a community challenge for fast calorimeter simulation, Rep. Prog. Phys. 88 (2025) 116201, DOI: 10.1088/1361-6633/ae1304

Development on Ultra-Long Wiring for Drift Chamber

[C02]

The 2026 International Workshop on the High Energy Circular Electron Positron Collider 21st-26th Oct.2026 Shanghai

Jing DONG Mingyi DONG Wenyu PAN Xiaohui QIAN

Institute of High Energy Physics, Chinese Academy of Sciences

Abstract

A drift-chamber-based design has been chosen and implemented as a possible alternative to the TPC, in order to contribute to the PID performance in the design of the CEPC reference detector[1].

On the one hand, the goal is to study and optimize the resolution of dN/dx with the advanced electronics and the multilayer DC prototype. Thanks to the fruitful collaboration with the Italian group[2], after the study of the simulation and the preliminary test, two short multilayer drift chamber prototypes have been developed and tested with the cosmic ray and the beam at CERN PS, respectively.

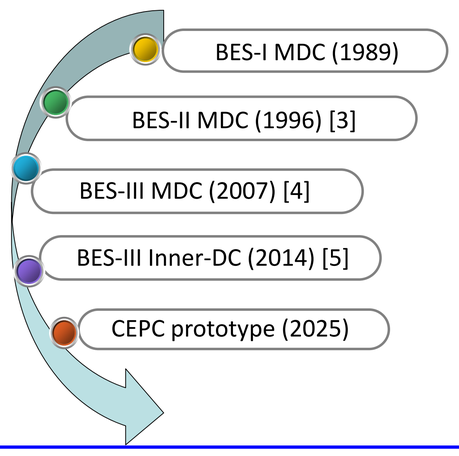
On the other hand, the goal is to explore conceptually long wiring, since there hasn't been any records or experience in the known experiments with such a 5.8-meter ultra-long drift chamber, especially used as fine as 20 μm Tungsten wire for the sense wire.

This work focuses on the latter and reports the progress on DC's ultra-long wiring. The following topics are addressed:

1) Mechanical tooling for measuring the ultimate tension has been optimized.
2) A tooling for ultra-long wiring has been designed and machined.
3) Unit arrays of wires as long as 5.3m have been wired, and the creep of the wires has been calculated.

Introduction

IHEP Drift Chamber:

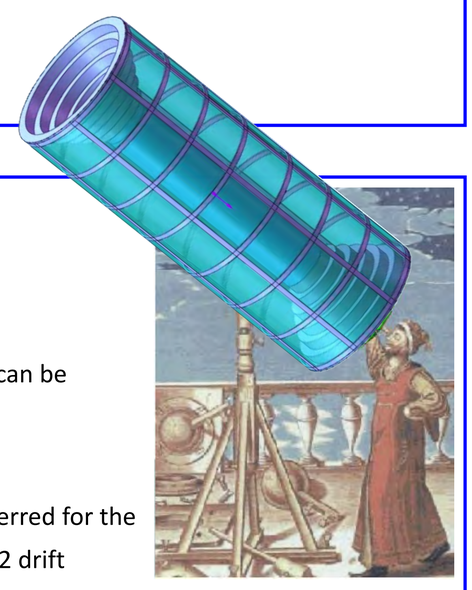


The CEPC Drift Chamber

- **Requirement for standalone momentum resolution: 10^{-4} (GeV/c)$^{-1}$ with a magnetic field of 3 T**
- Total Length : 5800mm
- Radial span : from 600 mm to 1800 mm
- Two CF cylinders + two endplates as a multi-stepped tilted profile
- Cell number : 27623 in total in 64 wire layers
- Cell size : 18 mm x 18 mm
- Ratio of field wires to sense wires: 3:1
- Wire: Tungsten 20 μm， Aluminum 80μm
- Gas mixture: He/iC4H10=90:10

- Use of cluster counting for particle identification

1. Simulation: shows that 3σ K/π separation at 20GeV/c can be achieved with 1.2m track length.
2. Electronics & prototype - scale DAQ: ready.
3. Construction: feed through and wire crimping are preferred for the wire anchoring system, as used in the BESIII and KLOE-2 drift chambers [6], both in operation for over 19 years.
4. Prototypes: two short multilayer ones are under study. Cluster counting reconstruction algorithm is under progress[7].



ZHAO Guang's talk & PAN Wenyu's poster

Wire

Wire

Wires:

- LUMA Tungsten NI-AU-PLT:20μm
- CFW Al5056 NI-AU-PLT: 80μm



Wiring

- Wire deflection :
  - ***Sag***: the maximum vertical drop of the wire, decided by the tension with this formula. $T(c) = \lambda L^2/(8S_{ag})$ (λ : Linear density, S_{ag} : Wire sag, L :Wire length)
  - ***Creep***: tendency of a solid material to deform permanently (stretch or change shape) under a sustained mechanical stress.
- Sagitta of ultra-long wiring: for the short chamber, tension can be performed from the designed sag, whereas the ultra-long wire chamber, the ultimate tension and creep, must be considered, and the deflection is then derived inversely, with the resulting sagitta affecting the spatial resolution.

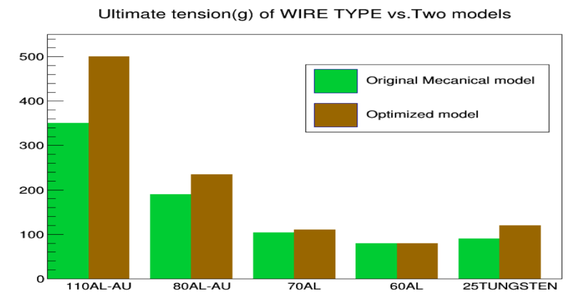
Ultra-long wiring: ultimate tension

1. The mechanical model for measuring the ultimate tension was machined as shown. However, after taking the measured values from this model into account, the optimal sag was around 700μm.

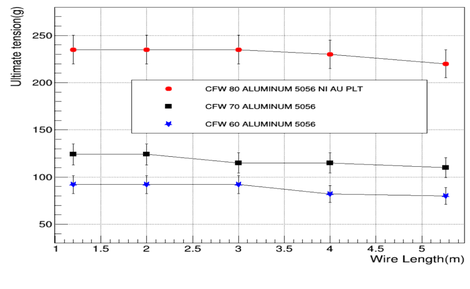
Importantly, in the BESIII MDC, the sag is approximately 80μm, compared with a spatial resolution of 130μm. The reconstruction algorithm and the overall DC design - by adding the stereo wire layers as in the BESIII MDC [4], to provide longitudinal measurements - help to minimize the impact of the sagitta on the spatial resolution.

2. Optimization was performed by replacing the wire supports on both sides, which significantly enhanced the ultimate tension, and corresponded to an optimal sag of about 300μm for a single wire.





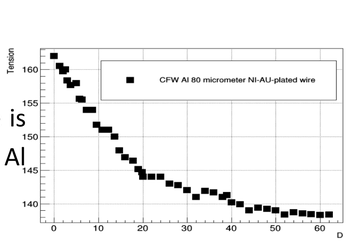
- The ultimate tension was measured for several wire lengths.
- Preliminary conclusion: within the range 1 - 5.3m, the ultimate tension is roughly constant，but decreases slightly as the length becomes ultra-long.
- The reason is not the material properties, but presumably to the weakening of the wire strength after slight damage, during the ultra-long wiring process .

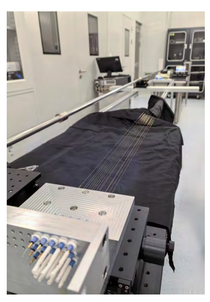


Ultra-long wiring: creep

- A tooling for ultra-long wiring has been designed and machined.
- Unit arrays of wires as long as 5.3m has been wired.
- The set tension and the tension after two months are 162 and 138g, respectively.
- For CFW Al 80μm NI-AU-plated wire，the creep ratio is less than 15%, creep time is around 2 months which is much shorter than that of the BESIII MDC wire(CFW Al 110μm NI-AU-PLT).
- It could be derived inversely by the final wiring，as shown in this formula:

$T(\iota) = T(Ultimate) \times C_2 \times (1+C_1)$， *where C_1 and C_2 correspond the creep and safety coefficient*, respectively.





Acknowledgments

The authors would like to thank BESIII-MDC and inner-DC group for the helpful record on the technology. This work was supported by the State Key Laboratory of Particle Detection and Electronics (SKLPDE-ZZ-202408).

Conclusion

1) For ultra-long wiring, the optimal sag of a single wire is around 300μm, which was greatly improved by optimizing the tooling. The creep of the field wire in the TDR[1] is less than 15%. Taking into account these numbers, the reconstruction algorithm and the future detailed design of CEPC DC - by adding the stereo wire layers to provide longitudinal measurements - will help to minimize the impact of the deflection on the resolution.
2) The feed through is reliable, since this is the first time that such a high tension achieved over such a long time. To meet the spatial resolution required by the CEPC design, the copper pin of the feed through may need to be optimized to achieve better anchoring.
3) Hand wiring is still unavoidable thanks to the feed through anchoring, but at least a robot for transferring the wire will be definitely necessary.
4) The creep of more type of wire will be calculated if needed, such as CFW-Al 60μmand CFW-Al 70μm wires used for the prototypes.

References

[1] CEPC Reference Detector Technical Design Report
[2] CEPC_workshop_Procacci,Barcelona,16Jun.2025
[3] Master thesis of Jundong Huang
[4] BESIII Preliminary Design Report, 2004
[5] Zhonghua QIN, https://arxiv.org/pdf/1312.0221
[6] KLOE drift chamber note from G.Bencivenni of INFN-LNF
[7] CEPC_workshop_Nicola De Filippis, Lisbon, 9Apr.2026

Particle Identification Studies using a Highly Granular Crystal ECAL

Jack Rolph, Yong Liu, Baohua Qi, Zhiyu Zhao
on behalf of the AGORA/CEPC Calorimetry Team

[C03]

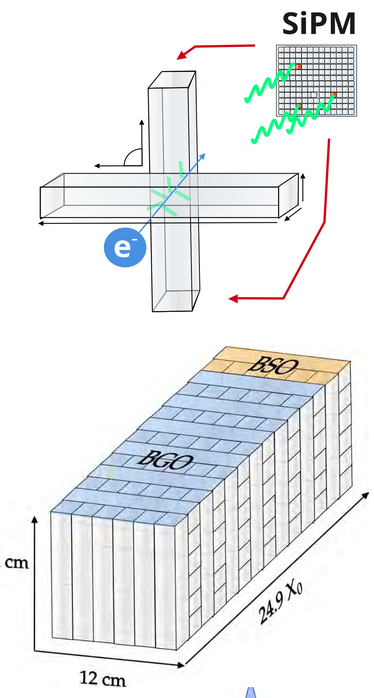
中国科学院高能物理研究所
Institute of High Energy Physics
Chinese Academy of Sciences

drdcalo

Overview

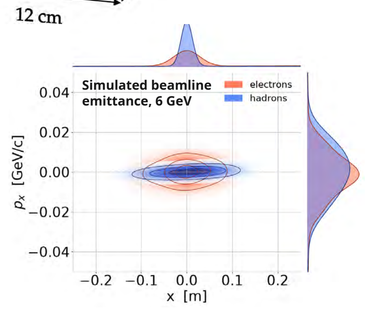
Highly Granular Crystal ECAL

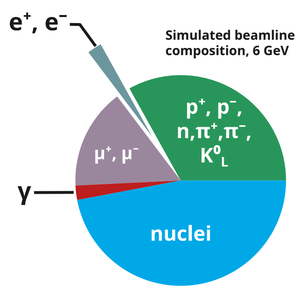
- **criss-crossing scintillating crystal bars [1]:**
  - CEPC detector volume: 1.5 × 1.5 × 40 cm³
  - prototype volume: 2 × 2 × 12 cm³
  - homogeneous;
  - crystal: BGO/BSO;
- **granularity:**
  - particle separation capability;
  - energy density information;
- **excellent EM energy resolution: stochastic term ~1-2%**



Particle Identification (PID)

- **Testbeam data contamination:**
  - Testbeam performed in June/July 2025;
  - Heavy contamination from hadrons;
  - Showering hadrons misidentified as electrons;
  - **influences energy resolution measurement;**
- **PID necessary for EM performance studies.**

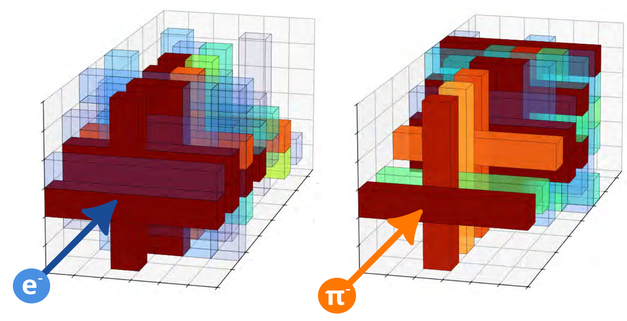




Summary of Studies

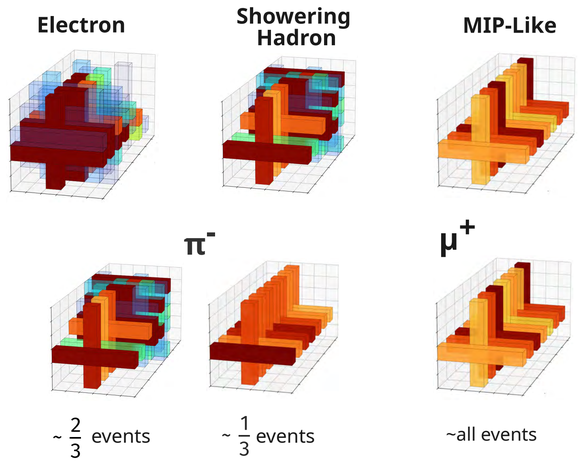
Simulation

- Geant4 simulation;
- DD4HEP geometry description;
- 1-10 GeV $e^-/\pi^-/\mu^+$ events;
- 130k μ^+ and 45k e^-/π events per energy;
- Detector effects (i.e., sensor noise).



PID: Unsupervised → Supervised

- **Three classes of event:**
  - electron;
  - showering-hadron-like;
  - MIP-like;
- **Problem: punch through hadrons:**
  - around 1/3 hadron events only ionize;
  - indistinguishable from μ^+/μ^-;
  - no trivial tag from simulation;
  - **empirical cut → classifier bias;**
- **Solution: unsupervised classification**
  - define measure where showering π^- is far from μ^+;
  - make cut to build tag;
  - **distill tag using simple classifier.**



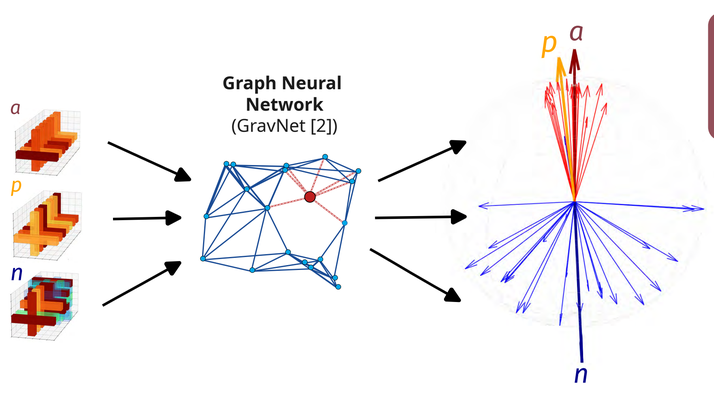


Key Results

Unsupervised PID: Contrastive Learning

- Sample two μ^+ events, and one π^- event;
  - **'anchor' (a_i)** : MIP-like reference event (μ^+);
  - **'positive' (p_i):** MIP-like event (μ^+);
  - **'negative' (n_i):** MIP-like / showering event (π^-);
- Encode each event to unit vector with neural network;
- Optimize triplet loss:

$$L(a,\ p,\ n) = \max\left\{d(a_i,\ p_i) - d(a_i,\ n_i) + \text{margin},\ \ 0\right\}, \qquad d(x_i,\ y_i) = \left\|\mathbf{x}_i - \mathbf{y}_i\right\|_2 = \sqrt{\sum_{k=1}^{D}\left(x_{i,k} - y_{i,k}\right)^2}$$

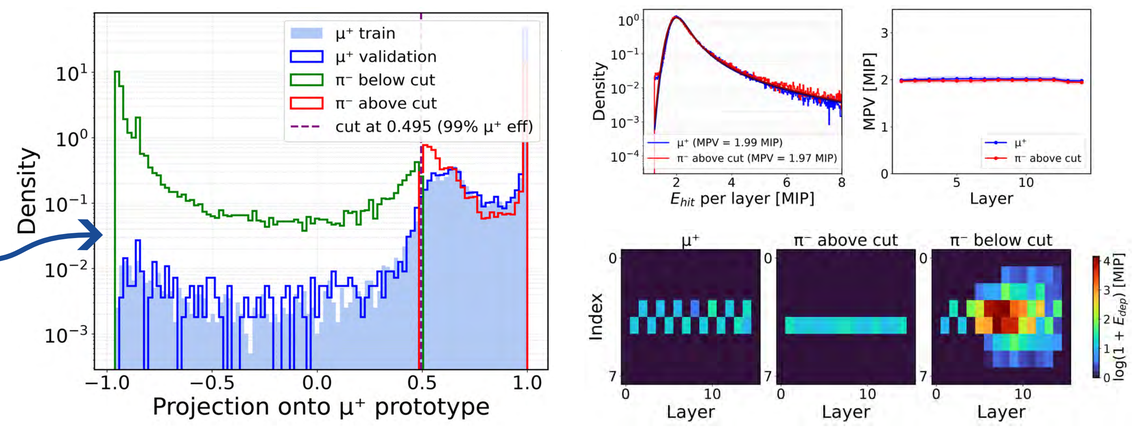


- Cosine similarity to average μ^+ vector ('prototype') from training data

→ 1D discriminator variable from 99% confidence interval of μ^+ projection.

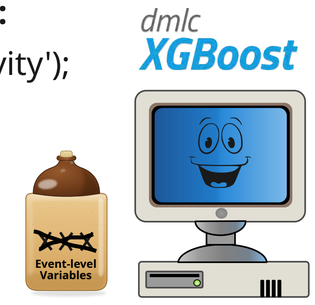
Key Result:

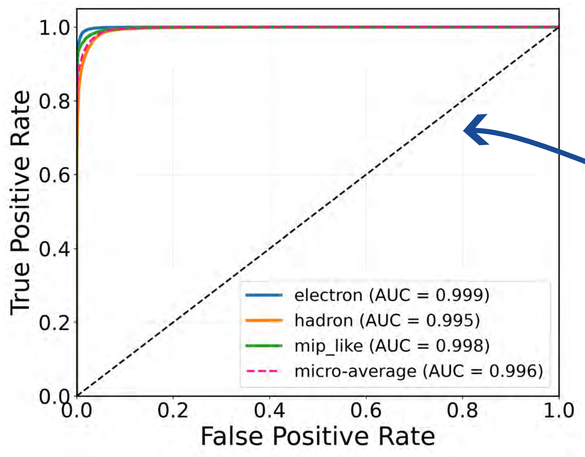
- **Red Region:**
  - Energy deposits Landau distributed;
  - ~ same MPV/layer as μ^+ ;
- **Green Region:**
  - Consistent with showering particle.



Supervised PID: Boosted Decision Tree

- **XGBoost gradient-boosted decision tree [3] (BDT) uses energy-independent event level variables:**
  - Energy-weighted mean position ('Center of Gravity');
  - Distance from Center of Gravity;
  - Fraction of energy per layer;
  - Moments of Central Log Ratio of bar energies;
- **BDT distills electron/showering hadron-like/ MIP-like from the unsupervised classifier.**



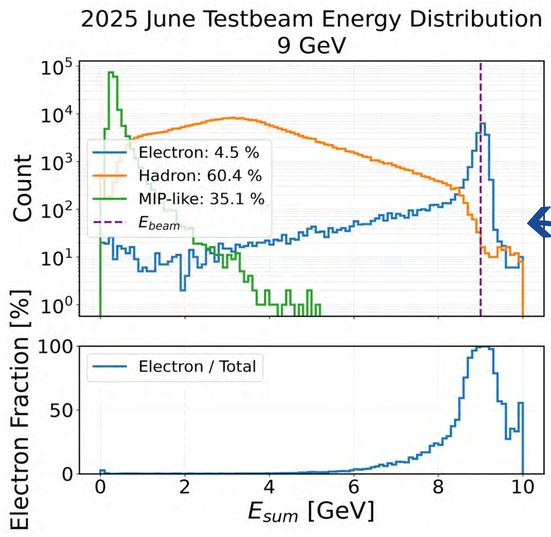


Key Result:

- Evaluation:
  e^-/μ^+: truth;
  π^-: unsupervised tag;
- Classifier performance almost perfect:

ROC AUC 0.996

- Consistent performance at all energies under test.
- Strong indication ECAL can be used for PID in Particle Flow.



Key Result:

- Applied to testbeam data;
- Classes of events follow expectations from experimental data;
- Electrons well-separated even though only 4.5% of total events.

[1] The CEPC Study Group, CEPC Technical Design Report -- Reference Detector, arXiv:2510.05260 [hep-ex] (2025), https://arxiv.org/abs/2510.05260.
[2] Qasim, S.R. et al., Learning representations of irregular particle-detector geometry with distance-weighted graph networks, Eur. Phys. J. C 79 (2019) 608, DOI: 10.1140/epjc/s10052-019-7113-9
[3] Chen, T. & Guestrin, C., XGBoost: A Scalable Tree Boosting System, Proc. 22nd ACM SIGKDD Int. Conf. Knowl. Discov. Data Min. (2016) 785–794, DOI: 10.1145/2939672.2939785

[C04]

Investigation of Time Projection Chamber Technology at Z operation for Future e^+ e^- Colliders

Jinxian Zhang[1] Xin She[1] Huirong Qi[1,†] Shengsen Sun[1,‡] Jianbo Zheng[1,2] Guang Zhao[1] Linghui Wu[1]
Haoyu Shi[1] Chengdong Fu[1] Gang Li[1] Manqi Ruan[1] Yue Chang[3] Jianchun Wang[1] Yifang Wang[1]

[1]Institute of High Energy Physics, CAS [2]University of Chinese Academy of Sciences [3]Central China Normal University

Introduction

The Time Projection Chamber (TPC) is the baseline main tracker for future lepton colliders (FCC-ee [1], CEPC [2], ILC), offering both **3D tracking** and **particle identification** (PID) via $\mathrm{d}E/\mathrm{d}x$ and cluster counting.

As a major scientific facility for future high-energy physics, the CEPC requires excellent PID for precision flavor physics. A core requirement is > 3σ separation between π and K up to 20 GeV/c [3]. The TPC must also achieve a standalone momentum resolution $\Delta(1/p_T) \sim 10^{-4}$ (GeV/c)$^{-1}$.

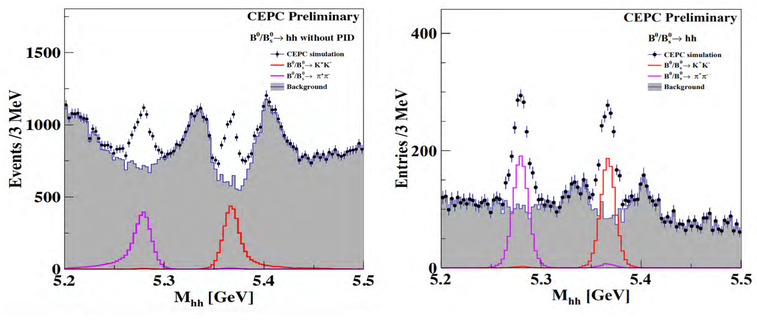


Figure 1. PID significantly reduces backgrounds in $B^0/B_s^0 \to hh$ decays, enabling clean separation of K^+K^- and $\pi^+\pi^-$ signals.

Particle Identification Performance & PID-Driven Design Optimization

TPC Baseline Design & Simulation Parameters

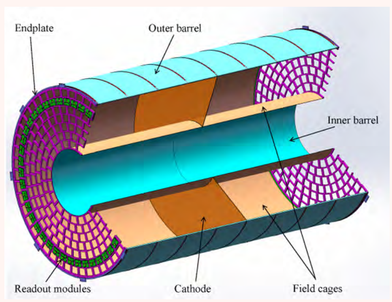


Figure 2. CEPC-TPC barrel design.

Table 1. Key TPC Parameters[3]

Parameter	Value
Inner/Outer radius	0.6/1.8 m
Max. drift length	2.75 m
Electric field	230 V/cm
Magnetic field	3 T
Working gas	T2K mixture (Ar:CF_4:iC_4H_{10} = 95:3:2)
Max. drift time	34 μs
Longitudinal/Transverse diffusion	265/30 $\mu\mathrm{m}/\sqrt{\mathrm{cm}}$
MIP ionization	$\sim$ 26 clusters/cm

Particle Identification Principle

The TPC traditionally measures ionization energy loss ($\mathrm{d}E/\mathrm{d}x$). With high-granularity readout, it can instead perform cluster counting, implemented as $\mathrm{d}N_\mathrm{p}/\mathrm{d}x$ — the number of activated pads per unit length. Both observables are reconstructed using a truncated-mean method. As demonstrated in CEPC Ref-TDR, the optimized $\mathrm{d}N_\mathrm{p}/\mathrm{d}x$ algorithm achieves better resolution and greater separation power than traditional $\mathrm{d}E/\mathrm{d}x$, with considerable potential for further improvement.

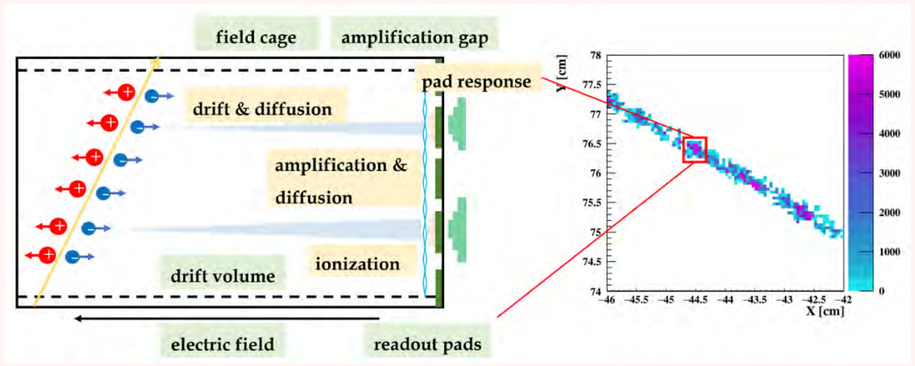


Figure 3. Schematic Diagram Illustrating the Operational Principle of the High-granularity Readout TPC.

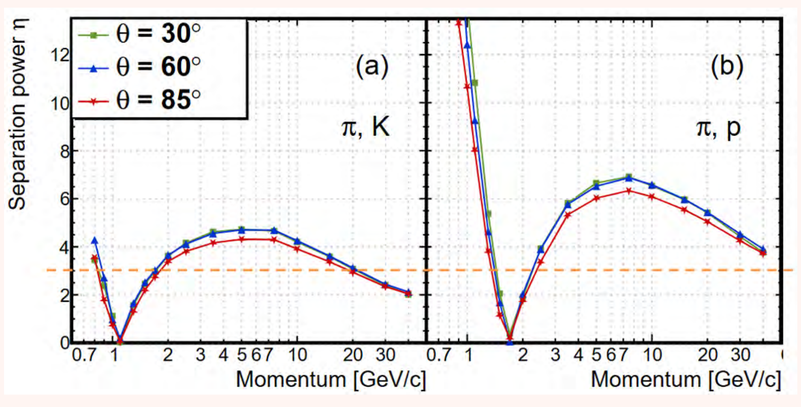


Figure 4. Separation Power of (a) π and K, (b) π and p.

Readout Pad Size Optimization

Our full-physics simulation study demonstrates that, after including drift and avalanche diffusion and applying the optimized truncated-mean reconstruction, the π/K separation power remains nearly constant for pad sizes $\leq 500\times500$ $\mu\mathrm{m}^2$, and clear PID degradation is observed only when pad size exceed 500 μm (Fig. 5). Therefore, the 500×500 $\mu\mathrm{m}^2$ pad is a reasonable choice, balancing excellent PID capability (achieving > 3σ separation up to 20 GeV/c) with reduced channel count and power consumption.

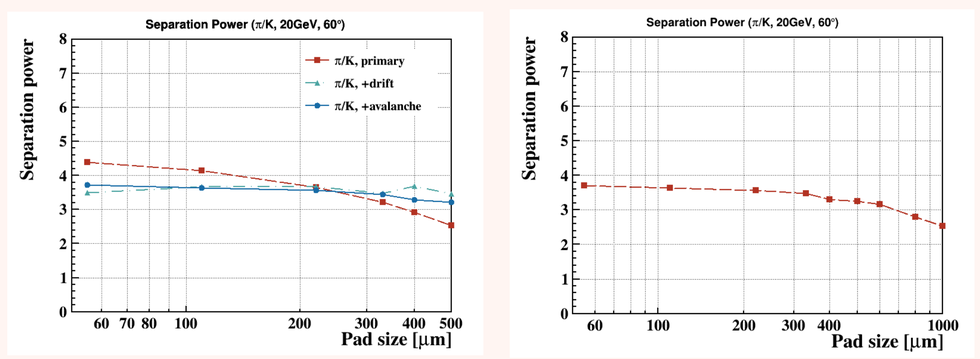


Figure 5. Separation power for pad sizes 55–500 μm (left) and extended to 1000 μm (right), at 20 GeV/c. Performance degrades above 500 μm.

Beam-induced background & space charge effect in the TPC

The Challenge: Space Charge at high luminosity Operation

A certain amount of beam-induced background (BIB) cannot be avoided when the CEPC operates at high luminosity modes. As shown in Fig. 6, these background particles ionize the TPC gas, producing slowly drifting positive ions that accumulate and distort the drift electric field — the **space charge effect (SCE)** — degrading momentum resolution.

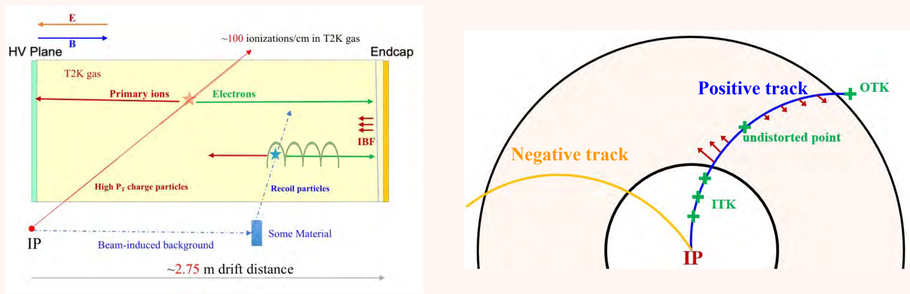
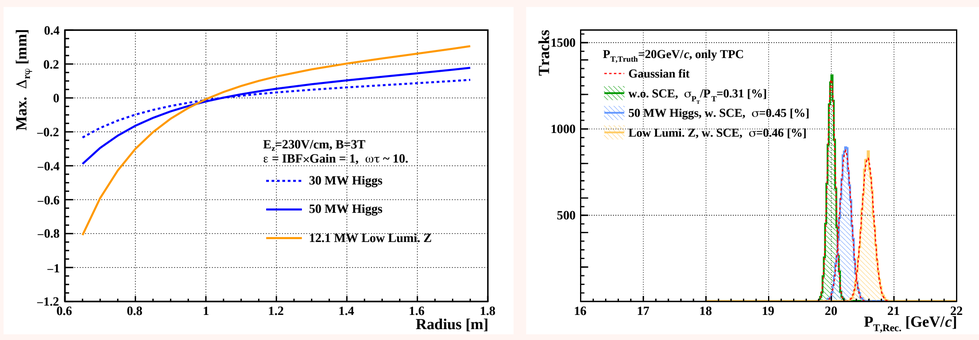


Figure 6. Sketch of beam-induced background and space charge effect in the TPC.

BIB Sources & Simulation Chain

Two categories of BIB are considered: **Beamstrahlung** (dominant, GuineaPig++) and **Single-beam** (BGS, BTH, Touschek).
Seeds → CEPCSW (Key4hep + Geant4) → space charge density map.

Deviations and impact on momentum measurement

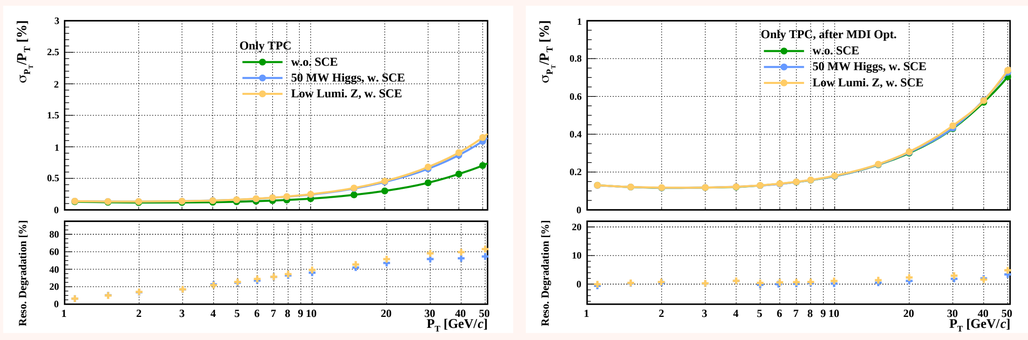


(a) (b)

Figure 7. (a) The maximum deviations in $r\varphi$ direction in different modes, (b) distributions of the transverse momentum of μ^+ particles reconstructed by the TPC.

- **Max. space charge density**: 1.6 nC/m^3 (50 MW H), 3.3 nC/m^3 (Low Lumi. Z).
- **Max. $\Delta_{r\varphi}$ @ 2.75 m drift**: 400 μm (H), 820 μm (Low Lumi. Z), as shown in Fig. 7 (a).
- Lead to straightening or bending of the tracks and deteriorated P_T resolution, see Fig. 7 (b).

Tracking performance w./w.o. MDI optimization



(a) (b)

Figure 8. Transverse momentum resolution versus P_T with the space charge effect. (a) pre-MDI optimization, (b) post-MDI optimization.

- Space charge degrades high-P_T ($\geq$ 10 GeV/c) reconstruction, as shown in Fig. 8 (a).
- Resolution drops >60% (@ 50 GeV/c) at low-luminosity Z running.
- Machine-Detector Interface optimization recovers TPC momentum resolution (Fig. 8 (b)), reducing max. space charge density below 1 nC/m^3 [4].

Summary & Outlook

1. **High-granularity TPC delivers excellent PID.** Sub-500×500 $\mu\mathrm{m}^2$ pad readout with optimized cluster-counting ($\mathrm{d}N_\mathrm{p}/\mathrm{d}x$) achieves $> 3\sigma$ π/K separation up to 20 GeV/c. Prototype beam tests are planned for experimental validation.
2. **High-luminosity Z-pole intensifies the space charge challenge.** Extrapolating from Low-Lumi. Z, the max. electron drift deviation could reach 2–3 mm, compounded by the magnetic field reduction from 3 T to 2 T. Advanced correction algorithms and MDI optimization are essential.
3. **Next:** prototype beam tests + refined simulations to develop and validate space-charge mitigation strategies for the high-luminosity Z-pole.

Acknowledgements: We thank the LCTPC international collaboration and experts Daniel Jeans, Paul Colas, Maxim Titov for their valuable help and discussions.

References

[1] I. Agapov et al. "Future Circular Lepton Collider FCC-ee: Overview and Status". In: Mar. 2022. doi: 10.48550/arXiv.2203.08310. arXiv: 2203.08310 [physics.acc-ph].

[2] The CEPC Study Group. "CEPC Technical Design Report: Accelerator". In: *Radiat. Detect. Technol. Methods* 8.1 (2024), pp. 1–1105. doi: 10.1007/s41605-024-00463-y. arXiv: 2312.14363 [physics.acc-ph].

[3] The CEPC Study Group. *CEPC Technical Design Report – Reference Detector*. 2025. arXiv: 2510.05260 [hep-ex]. url: https://arxiv.org/abs/2510.05260.

[4] Xin She et al. "Simulation studies of beam-induced background and space charge effects on Time Projection Chamber for the CEPC". In: *The European Physical Journal Special Topics* (2026). issn: 1951-6401. doi: 10.1140/epjs/s11734-026-02404-w.

Study of Cluster Counting Method for CEPC Drift Chamber

Wenyu Pan[1,2], Mingyi Dong[1,2], Dongcheng Cai[1,2,3], Jing Dong[1,2], Mengyang Ji[1,2], Liangchenglong Jin[1], Hongbin Liu[1,2,3], Xiaoyan Ma[1,2], Xiaohui Qian[1,2], Linghui Wu[1,2], Wan Xie[1], Dewei Xu[3,4], Hongyu Zhang[1,2], Guang Zhao[1,2], Yubin Zhao[1,2,3]

[C05]

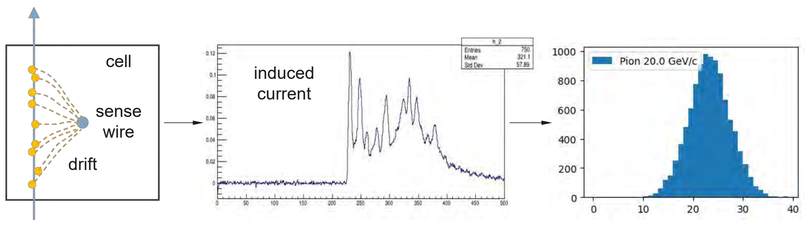
[1]Institute of High Energy Physics, Chinese Academy of Sciences, Beijing 100049, P. R. China
[2]University of Chinese Academy of Sciences, Beijing 100049, P. R. China
[3]Spallation Neutron Source Science Center, Dongguan 523803, Guangdong, P. R. China
[4]Dongguan University of Technology, Dongguan 23808, Guangdong, P. R. China

Abstract

Flavor physics and jet measurements at CEPC impose stringent particle-identification requirements. A drift chamber using primary ionization cluster counting (dN/dx) is a promising tracker option; simulations indicate that an optimized dN/dx chamber can achieve K/π separation exceeding 3σ up to 20 GeV/c. We developed a multi-channel prototype with gold-plated tungsten sense wires and aluminum field wires, compatible with the CEPC drift chamber design. A 1.3 Gsps high-bandwidth, low-noise readout and DAQ system ensures faithful multi-channel capture of fast ionization signals, providing an experimental foundation for dN/dx studies. Commissioning and cosmic-ray tests confirmed electronics performance and reliable operation. Beam tests with muon, pion, and kaon beams validated the hardware and will evaluate dN/dx PID capability, guide optimization of the CEPC drift-chamber technical design and parameters, and inform further hardware improvements.

Introduction

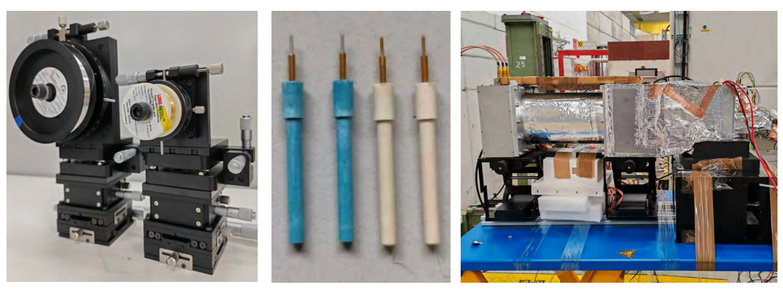
- A drift chamber acts as an alternative gaseous detector for CEPC, delivering superior particle identification (PID) and accurate tracking.
  - Layout: R = 600-1800 mm, length 5800 mm, cell ~18 mm×18 mm, 64 wire layers, ~27 k cells, field-to-sense wire ratio 3:1.
  - Wires: sense 20 μm gold-plated tungsten, field 80 μm gold-plated aluminum
  - Gas: He:iC_4H_{10} = 90:10.
- The flavour physics and jet programme at CEPC calls for more stringent particle identification; dN/dx offers significantly better resolution (2-3%) than the conventional dE/dx approach (5-6%).

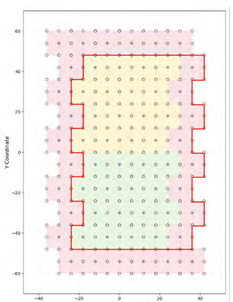


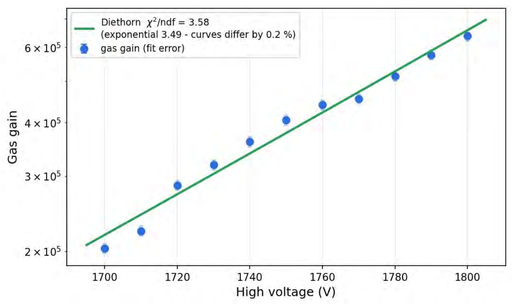
- The quantity dN/dx represents the primary ionization cluster count per unit track length within the drift chamber, the measurement of which presents several challenges in hardware.
  - Challenge 1: Sufficient time interval between different ionization signals and reduce interference between different ionization clusters. → Detector optimization includes cell size and gas.
  - Challenge 2: Fast signal shaping speed and high SNR. → Readout electronics with low noise, high bandwidth, high sampling rate.

Multi-layer drift chamber

- The prototype has 6 layers of 10 cells each (total 60 cells), cell size 12 mm×12 mm, length 25 cm
- 60 sense wires: 20 μm Au-plated tungsten, tension 4.79 g, sag 10 μm
- 222 field wires: 70 μm aluminum, tension 8.07 g, sag 10 μm
- The wires are fixed by crimping the feedthroughs
- All channels are split into three groups and routed to three high-voltage channels to ensure consistent gain





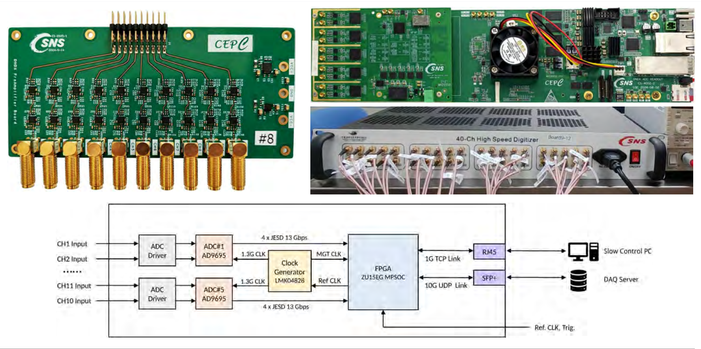


- HV scan
  - Gain calibration with a ^{55}Fe source at He:iC_4H_{10}=90:10 gas mixture
  - Gas gain versus high voltage fitted with the Diethorn two-parameter formula.
  - Optimal cluster-counting range: 1×10^5–5×10^5 (HV1700–1800 V).

High-speed readout electronics

- Fast front-end current preamplifier
  - Circuit structure: Two-stage non-inverting amplifier with LMH6629 wideband op-amps.
  - Gain performance: Equivalent transimpedance gain 1233 Ω (voltage gain of 24.66 V/V).
  - Measured bandwidth and noise: Analog bandwidth of 601 MHz, baseline noise 1.09 mVrms.
- Digitization electronics
  - Heterogeneous architecture: AD9695 ADC board + ZU15EG FPGA board.
  - High-speed digitization: Sampling rate 1.3 GSps, resolution 14 bit.
  - Link integrity: The fiber-optic link runs error-free continuously at 10 Gbps. Eye opening 55.56%.

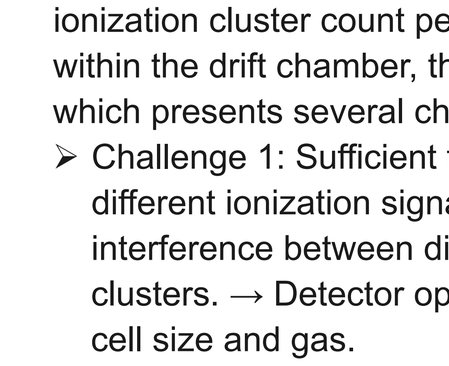
Further details: Hongbin Liu's talk

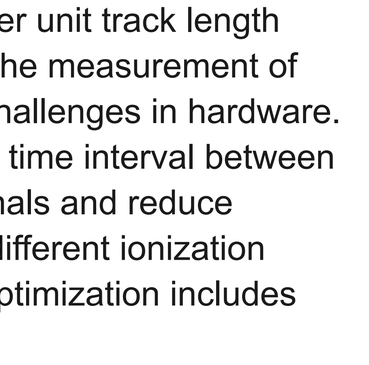


Performance metrics	Measured
Transimpedance gain	1233 Ω
Full-chain bandwidth	550 MHz
Linear dynamic range	660 μA
Equivalent input noise	0.81 μA_rms
ADC sampling rate	1.3 GSps
ADC quantization precision	14-bit
Time measurement precision	0.88 ns

Testbeam system set up

Schematic diagram of the beam test system

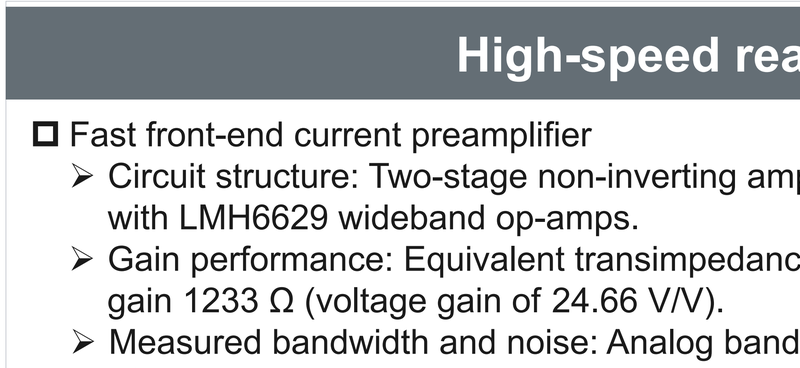




- A joint beam test with the INFN IDEA DCH group was conducted at CERN PS T9 in June 2026
- 416 GB data including Muon (2, 4, 6, 8, 10,12 GeV/c), Kaon (6, 10 GeV/c) and Pion (6, 10 GeV/c).

Preliminary results

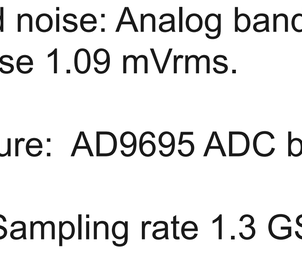
- System characterization



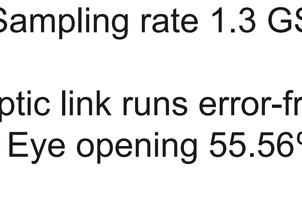
The waveform and the peaks identified using the second-derivative method.

Pion 10GeV

- dE/dx
  - The dE/dx resolution for an equivalent 1 m track is approximately 4% at a 15% truncation fraction.



- dN/dx
  - The machine-learning-based reconstruction algorithm achieves a resolution of 3.51%.



Further details: Guang Zhao's talk

Summary & outlook

- A dN/dx test system constructed, including the multi-layer drift chamber, readout electronics, and DAQ.
- Joint commissioning of the test system has been completed, and beam tests have been carried out at CERN.
- The dN/dx results of beam data are currently being analyzed, and the reconstruction algorithms are under development.
- Optimization of the detector design and readout electronics architecture.

References

[1] CEPC Reference Detector Technical Design Report, arXiv:2510.05260
[2] W. Elmetenawee et al 2025 JINST 20 P11019
[3] Cai D. C., et al., 2026, Radiat. Detect. Technol. Methods, doi:10.1007/s41605-026-00712-2

[C06]

Performance Evaluation of Stereo ECal Prototype

Bingkun He[1,2], Huaqiao Zhang[1,2]

[1]Institute of High Energy Physics, CAS, Beijing, China [2]University of Chinese Academy of Sciences

Concept and Prototype of Stereo ECal

Motivation

Conventional crystal ECALs provide fine segmentation in z and ϕ, but typically only one radial segment, limiting longitudinal sampling and 3D tracking capability.

Concept

- Crystals do not point directly to the IP, but are tilted by a pointing angle α.
- Radial sampling layers provide **multiple shower-depth measurements.**
- Adjacent layers adopt opposite (+α/−α) stereo orientations.
- **Single-ended 2D readout** + stereo geometry → **3D position reconstruction**

Physics Goal

Energy resolution + 3D positioning + shower separation
for FCC/CEPC Higgs / electroweak precision measurements and PFA

Advantages over the CEPC Baseline Design

1. **Self-Supporting Structure**
2. **Less Dead Area**
3. **Fewer Ghost Hits**
4. **Better Suited for Machine-Learning-Based Reconstruction**



Prototype Photo

SiPM: S14160-6050HS



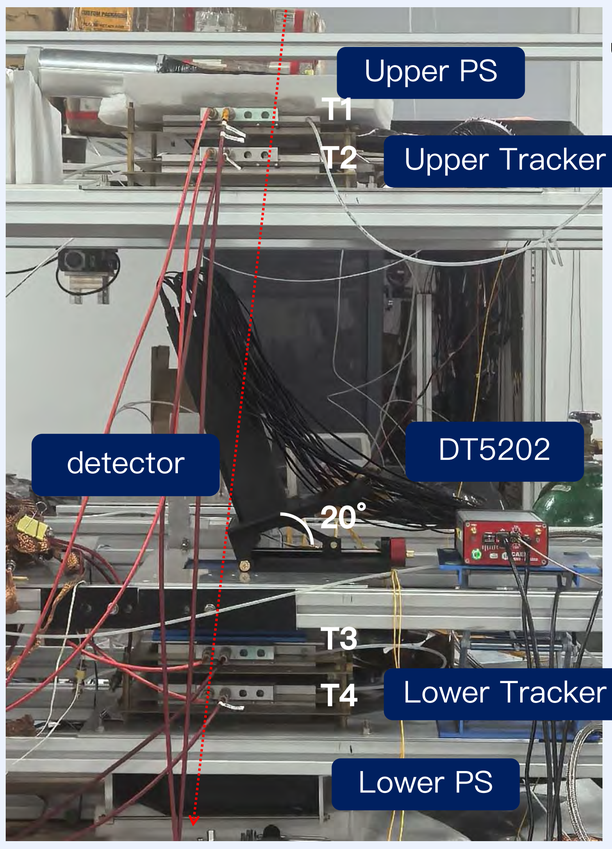
Readout from the outer side, away from the IP



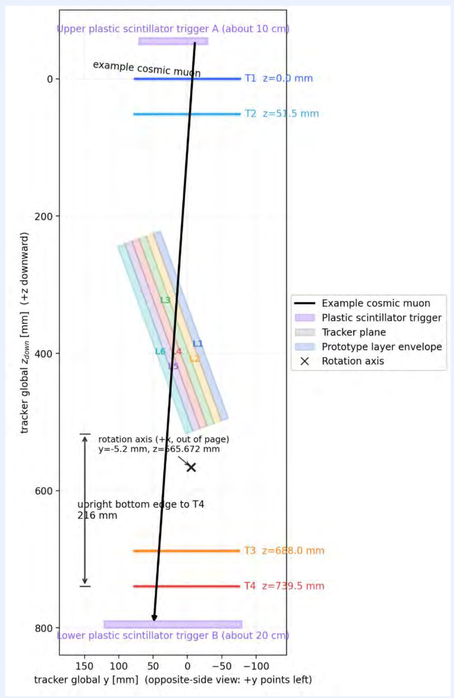
The electronic system is based on **CAEN DT5202**

Note: BGO crystals are replaced by plastic scintillators, since BGO crystals are expensive and this test focuses on **spatial-resolution measurements**.

Cosmic Test Setup

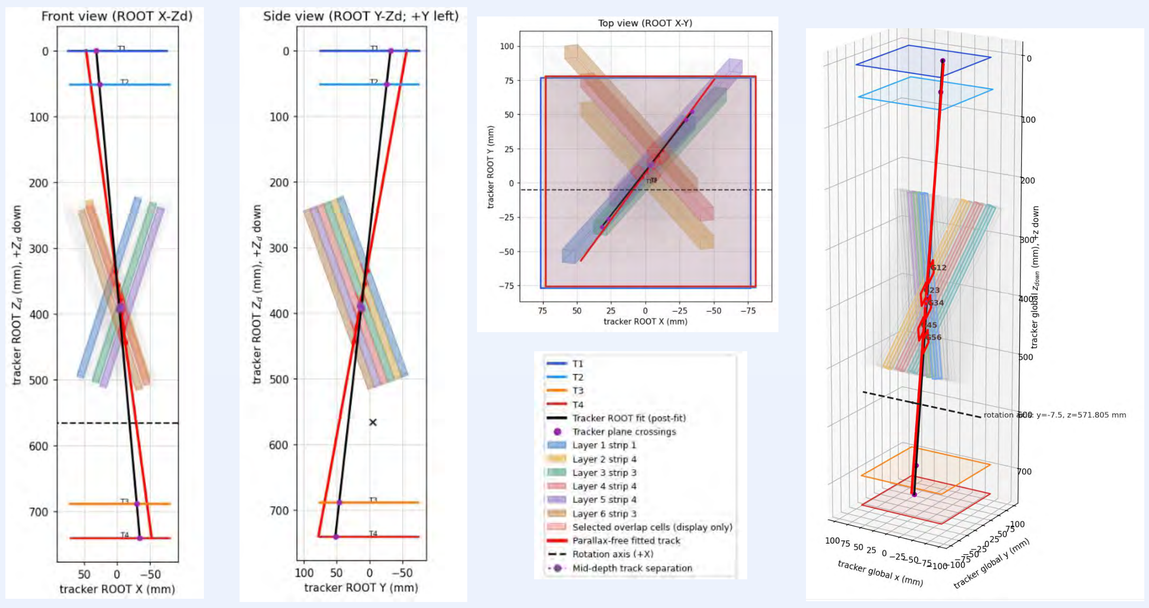


T1–T4 are four gaseous wire-chamber trackers used to reconstruct the reference cosmic-ray tracks.



Prototype performance is evaluated by comparing tracker-reconstructed and prototype-reconstructed cosmic-ray tracks.

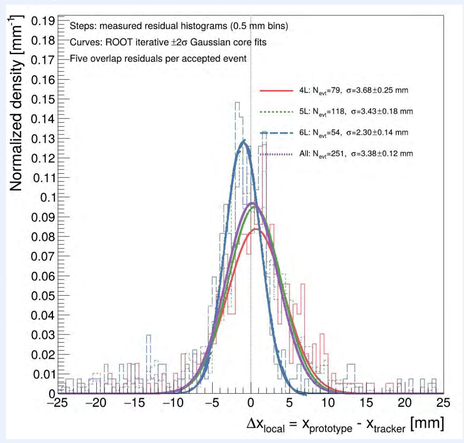
Typical Cosmic Muon Event



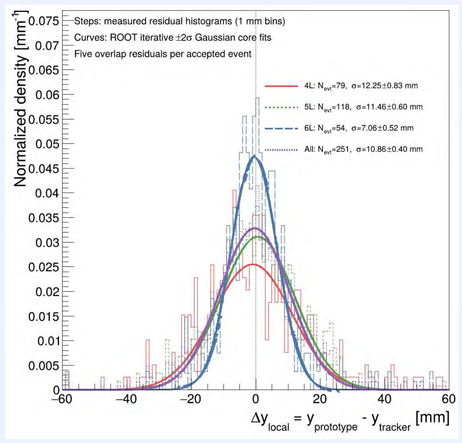
Reconstructed Tracks (red) show good correlation with the **Reference Tracks (black)**.

x and y Spacial Resolution

x Spatial Residual Distribution



y Spacial Residual Distribution



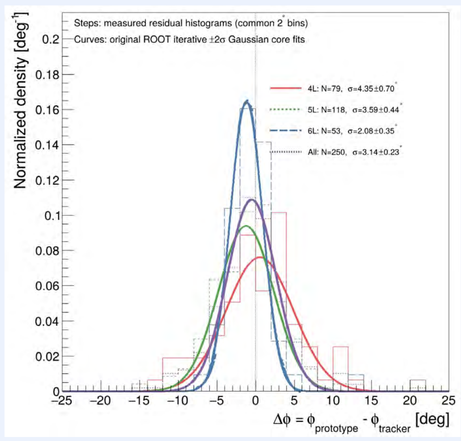
For events with hits in all 6 layers

x spatial resolutions:
2.30±0.14mm

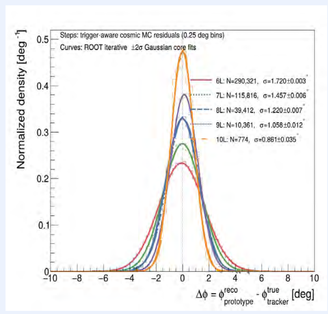
y spatial resolutions:
7.06±0.52mm

ϕ Angular Resolution

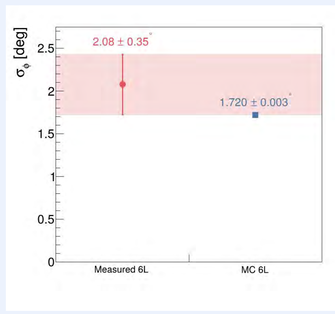
ϕ Angular Residual Distribution (measurement)



ϕ Angular Residual Distribution (MC)

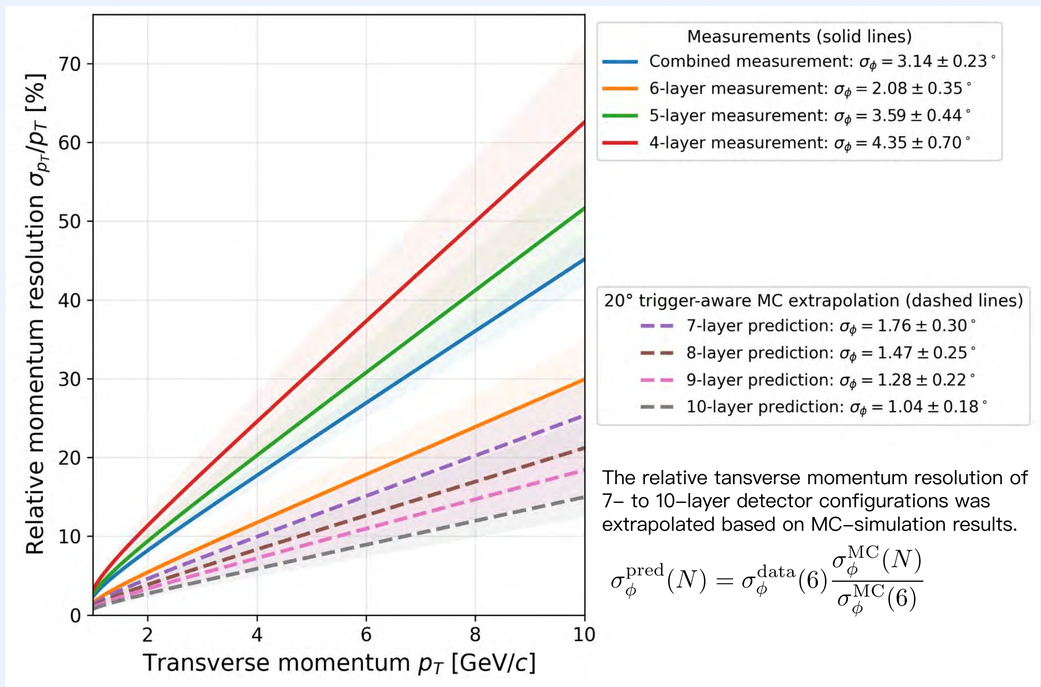


MC-simulated ϕ angular resolutions for 6- to 10-layer detector configurations.



For the 6-layer, the MC prediction agrees well with the measured angular resolution within uncertainties.

Momentum Resolution Extrapolation



The relative tansverse momentum resolution of 7- to 10-layer detector configurations was extrapolated based on MC-simulation results.

$$\sigma_\phi^{\mathrm{pred}}(N) = \sigma_\phi^{\mathrm{data}}(6)\frac{\sigma_\phi^{\mathrm{MC}}(N)}{\sigma_\phi^{\mathrm{MC}}(6)}$$

$\frac{\sigma_{p_T}}{p_T} \approx 15\%$ at $p_T = 10\mathrm{GeV/c}$ for 10 layers prototype.

Conclusion & Outlook

Summary

✓Measured the prototype spatial resolution and the ϕ angular resolution: 3.38 ± 0.12 mm (x) , 10.86 ± 0.40 mm (z) and 3.14 ± 0.23 degree (ϕ).

✓MC-based extrapolation predicts a clear improvement in momentum resolution with increasing layer number, reaching $\sim 15\%$ at $p_T = 10\mathrm{GeV/c}$ for 10 layers prototype.

✓This study demonstrates the potential of Stereo ECal for charged-particle track reconstruction and momentum measurement.

Outlook

➢ **Prepare Crystal prototype**
Complete the assembly of the crystal prototype for subsequent detector tests.

Email: hebk@ihep.ac.cn

中国科学院高能物理研究所
Institute of High Energy Physics, Chinese Academy of Sciences

Performance Study of BSO Crystal Bars for High-Granularity Electromagnetic Calorimeters

Yushan Liu, Yong Liu, Baohua Qi, Dejing Du
on behalf of the CEPC-calorimetry team

Institute of High Energy Physics, Chinese Academy of Sciences

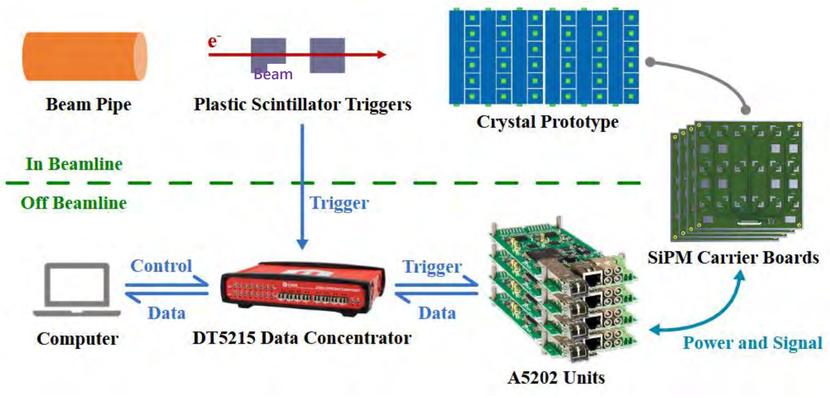
01 Motivation & Concept

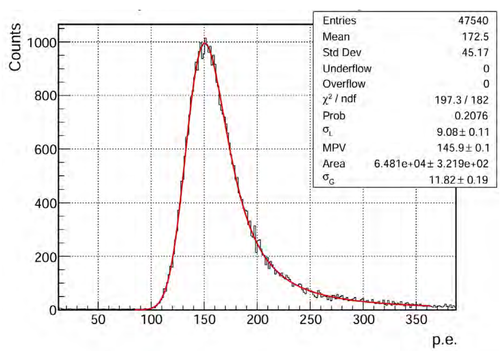
Crystal ECAL for future e^+e^- colliders

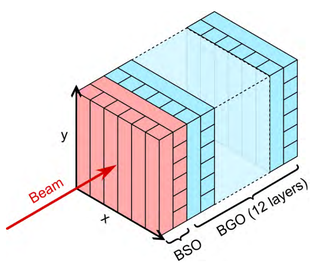
- **BSO as an alternative [1,2,3]**
  - Faster scintillation
  - Potential cost benefit
- **ECAL Design**
  - 15 × 15 × ~400 mm³ bars
  - Orthogonal layers with two-ended SiPMs

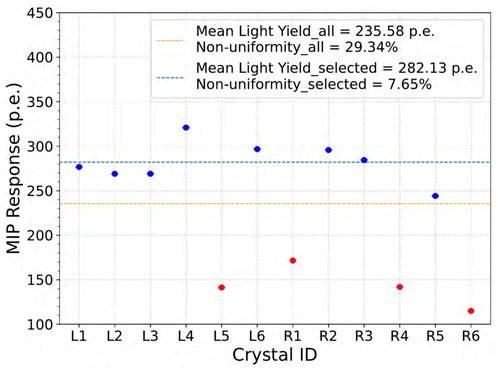
Typical crystal properties [4]

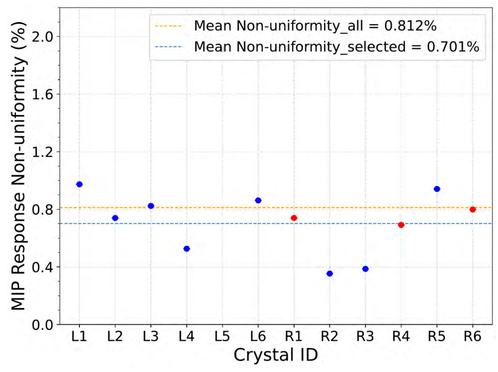
Property	BSO($Bi_4Si_3O_{12}$)	BGO($Bi_4Ge_3O_{12}$)
Density (g/cm³)	6.80	7.13
Radiation length (cm)	1.15	1.12
Decay time (ns)	100	300
Emission peak (nm)	470	480
Light yield (ph/MeV)	1/5-1/4 of BGO's	8000-10000











02 CERN PS-T9 Beam Test

- ✓ **12 BSO bars, 20 × 20 × 120 mm³**
- ✓ **10 GeV pion beam**
- ✓ **6 × 6 scan with 2 cm step**
  - MIP selection: one hit bar per layer
  - Fit: Landau function convolved with Gaussian
  - MPV as MIP response

➢ **Light yield: 282 p.e./MIP**

➢ **Non-uniformity**:

<1% intra-bar

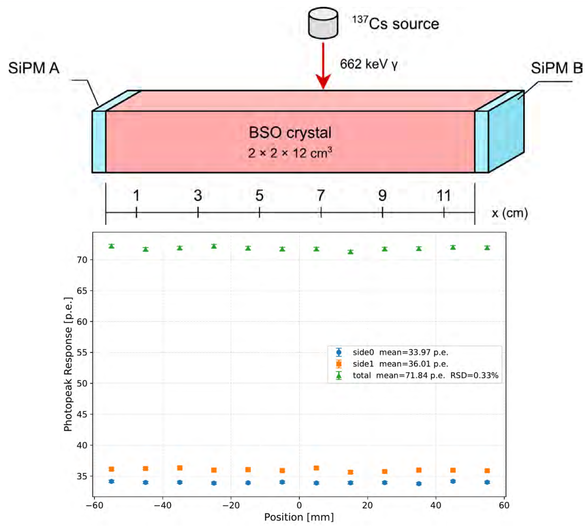
7.65% inter-bar

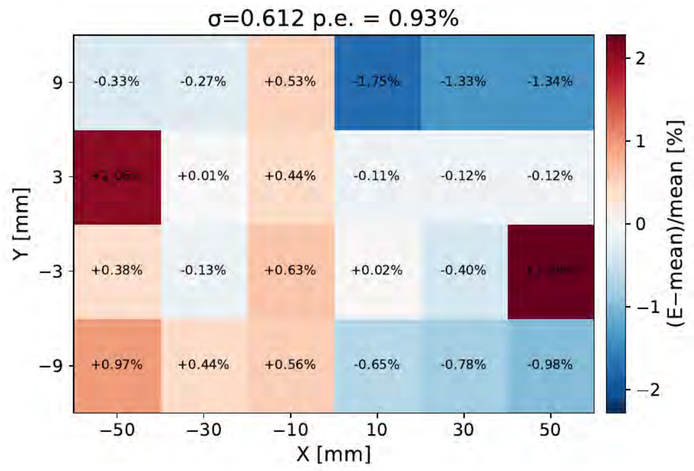
03 Laboratory Experiment

- ✓ Collimated ^{137}Cs · 662 keV γ
- ✓ Longitudinal scan: 12 positions
- ✓ Two-dimension scan: 6 × 4 positions

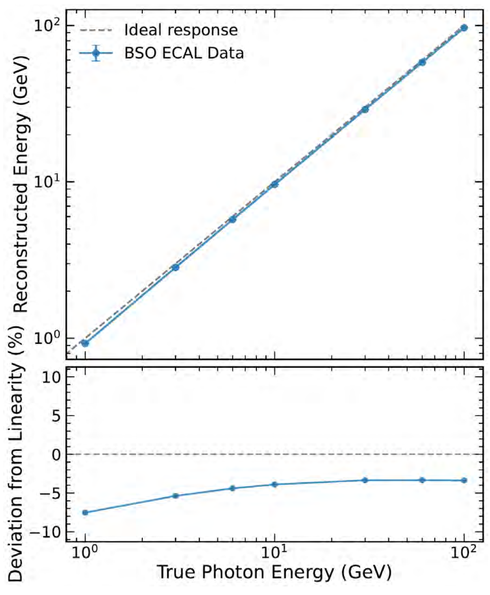
➢ **Non-uniformity < 1%**

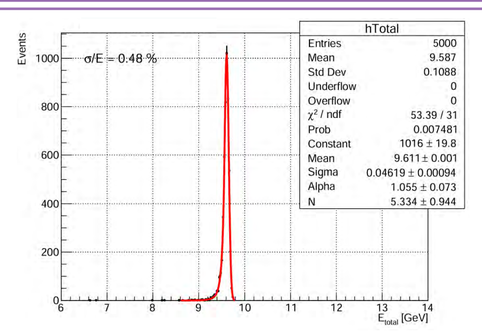
Consistent with beam-test, excellent uniformity!

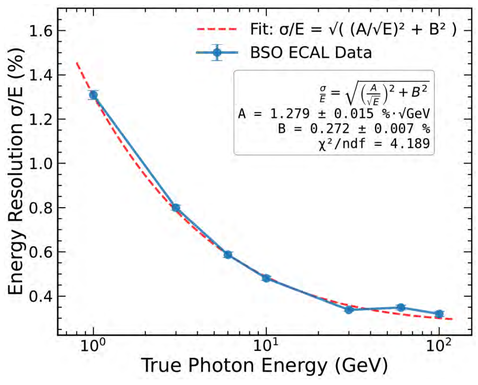




04 Detector Simulation







- ✓ **Geant4 of BSO crystal ECAL with 405mm bars**
  Incident particle: 1–100 GeV photons
- ✓ **Digitization**
  - Light yield 282 p.e./MIP
  - Poisson statistics
  - 1% non-uniformity

➢ **Crystal Ball Fit → Energy Resolution (MC Truth)**

σ/E = 1.28%/√(E/GeV) ⊕ 0.27%

Excellent energy resolution for EMC!

Conclusions

- Sub-percent intra-bar non-uniformity of BSO
- Simulation supports BSO as an ECAL candidate

Outlook

- Crystal quality control & bar-by-bar calibration
- BSO ECAL prototype validation

[1] CEPC Reference Detector TDR, arXiv:2510.05260 (2025). [2] F. Yang et al., J. Phys.: Conf. Ser. 587 (2015) 012064. [3] M. Deng et al., IEEE Trans. Nucl. Sci. 73 (2026) 1535-1542.
[4] R.-Y. Zhu, Recent Progress on Inorganic Scintillators for Future High Energy Physics Experiments, SPIE (2021), slide 15.

CEPC Workshop 2026 [C08]

中国科学院高能物理研究所
Institute of High Energy Physics, Chinese Academy of Sciences

Experimental Characterization and Optical Simulation of Scintillating Glass for the AGORA Calorimeter

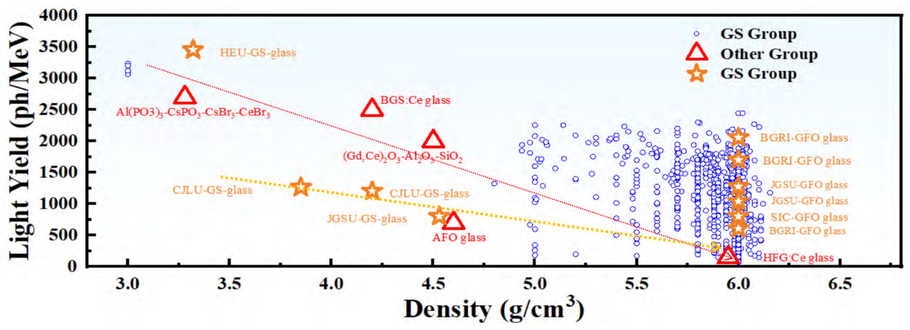
Yushan Liu, Yong Liu
on behalf of the AGORA-calorimetry team

Institute of High Energy Physics, Chinese Academy of Sciences

01 Background

AGORA: one of the detector concepts proposed for FCC-ee

- Material cost of crystal ECAL motivates a glass alternative.
- Improved GFO glass motivates extending scintillating glass to ECAL.
- ECAL material-cost savings allow a larger sensitive volume in HCAL.



Design requirements

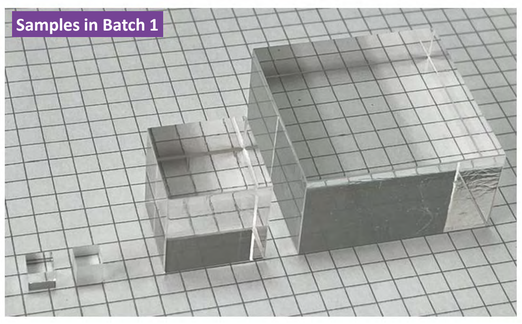
Property	ECAL	HCAL
Density (g/cm³)	6.0	6.0
Light yield (ph/MeV)	2000	≥1000
Attenuation length (cm)	≥10	≥10
Scintillation time (ns)	~500	~500

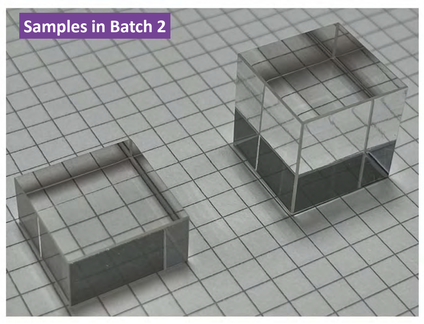
Section	CEPC Reference detector	AGORA concept
ECAL	BGO crystal bars	Finely segmented GFO glass cells
HCAL	Glass + steel sampling ~30% sampling fraction	Glass replaces steel absorber High active material fraction

02 Laboratory Cosmic-Ray Test of Scintillating Glass Samples

ScintGlass samples from BGRI:

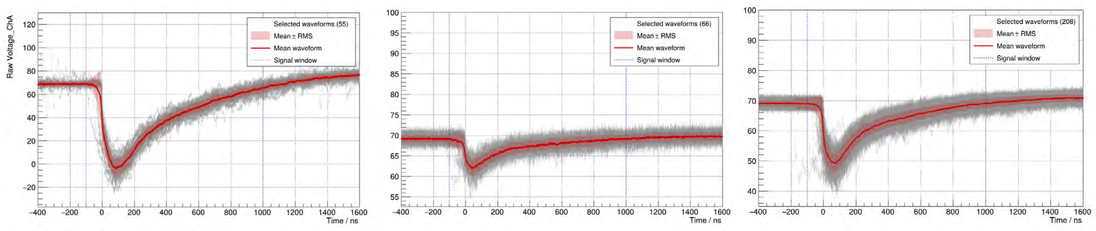
- Batch 1: 5×5×5 mm³ cube × 2, **20×20×20 mm³ cube**, 40×40×20 mm³ brick
- Batch 2: **20×20×10 mm³ tile, 20×20×20 mm³ cube**





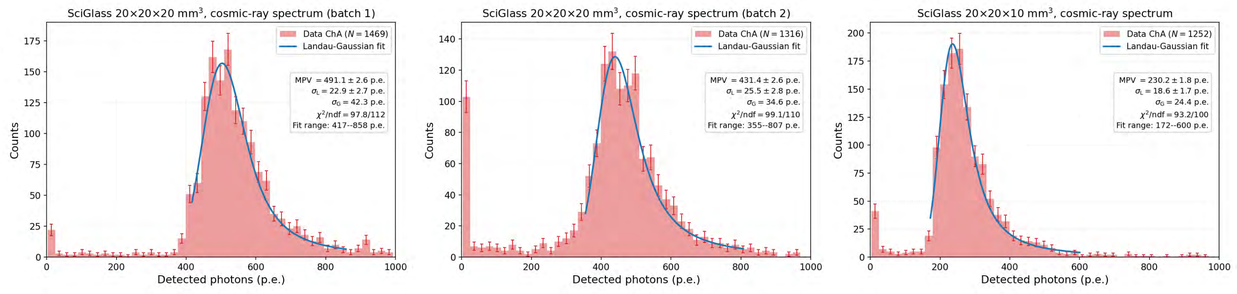
Typical cosmic-ray waveforms of ScintGlass with different SiPMs:

S13360-6025PE S14160-3010PS S14160-3015PS



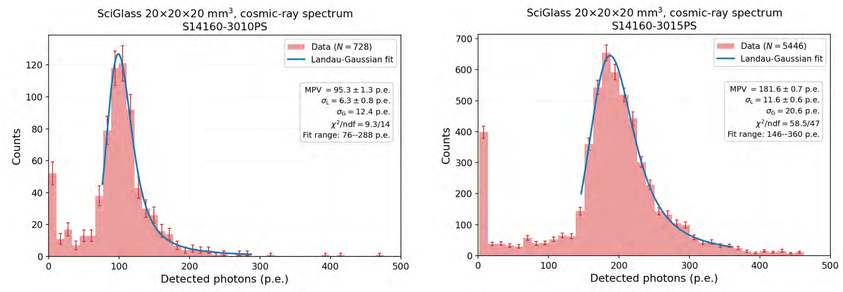
MIP response results from cosmic-ray test:

- 3 different samples with 6×6 mm² SiPM (Hamamatsu S13360-6025PE)



MPV: 491.1 ± 2.6 p.e. MPV: 431.4 ± 2.6 p.e. MPV: 230.2 ± 1.8 p.e.

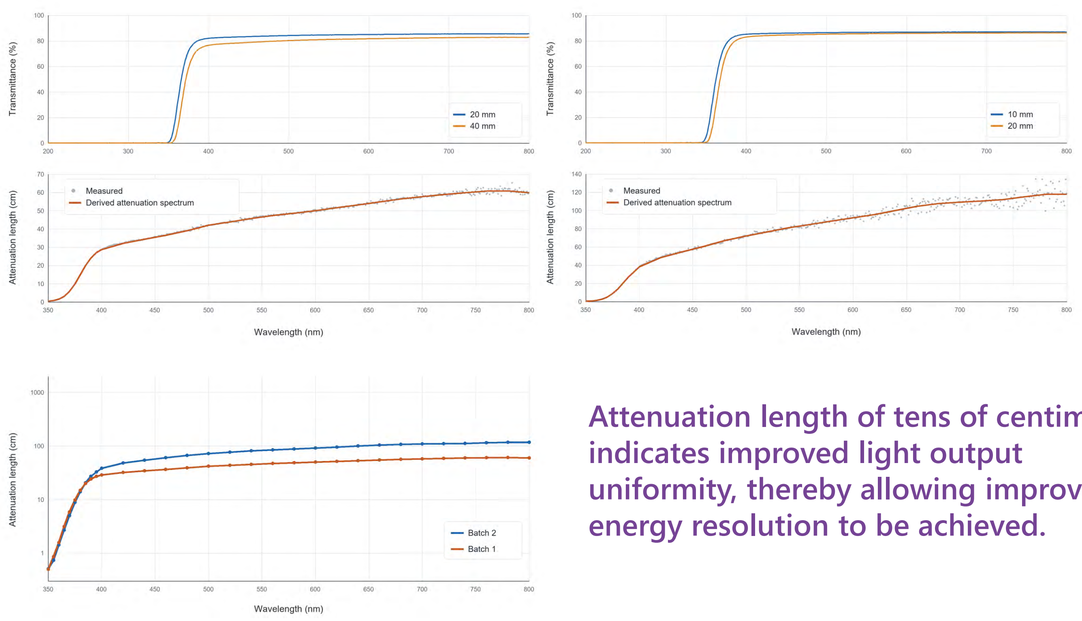
- 1 sample with different 3×3 mm² SiPM (Hamamatsu S14160-3010PS, S14160-3015PS)



MPV: 95.3 ± 1.3 p.e. MPV: 181.6 ± 0.7 p.e.

03 Transmittance and Attenuation Length

- Measurements of transmittance(T) by Agilent Cary 60 UV-Vis spectrophotometer
- Culculation of the attenuation length: AL = (L1-L2)/ln(T2/T1)

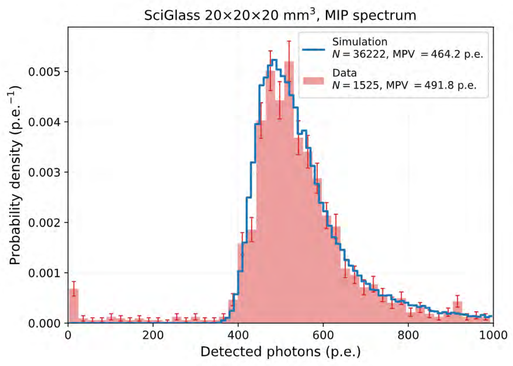


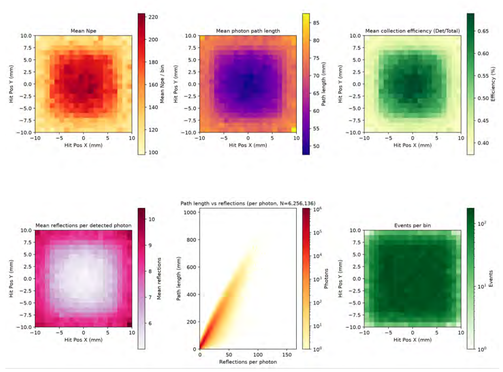
Attenuation length of tens of centimeters, indicates improved light output uniformity, thereby allowing improved energy resolution to be achieved.

04 Optical Simulation

Developing a Geant4 optical model to describe and understand the optical properties of ScintGlass

- The established model has been initially validated against a specific set of experimental data, providing a basis for further refinement.
- To identify the best model, the next step is to tune parameters such as light yield and attenuation length and to introduce scattering, so that the simulation agrees with all measured data.





Conclusions

- Light output of 95–491 p.e./MIP, providing promising photon statistics for ECAL
- Wavelength-dependent attenuation length on the order of tens of centimeters
- Providing encouraging reference results for future R&D

Outlook

- Position-dependent light output uniformity scan
- More rigorous calculation of attenuation length
- Further optimization of the Geant4 optical model

[1] CEPC Reference Detector TDR, arXiv:2510.05260 (2025).

[C09]

CEPC 2026

Oct.22-26,Shanghai, China

Toward Large-Diameter BaF_2:Y Scintillators with Controlled Light Response: Crack-Free Crystal Growth and Optical-Transport Diagnostics

Jing Zhang[1,2], Xiang Li[1], Jiawei Xu[1], and Junfeng Chen[1,2*]

1. State Key Laboratory of Functional Crystals and Devices, Shanghai Institute of Ceramics, Chinese Academy of Sciences, Shanghai, China;
2. Center of Materials Science and Optoelectronics Engineering, University of Chinese Academy of Sciences, Beijing, China

**Corresponding author: jfchen@mail.sic.ac.cn*

Abstract

➢ Yttrium-doped barium fluoride (BaF_2:Y) is attractive for high-rate radiation detection because Y doping suppresses the slow self-trapped-exciton emission while retaining the ultrafast core-valence luminescence of BaF_2. Its practical use, however, requires both scalable crystal growth and control of position-dependent light collection. We address these requirements through two complementary studies using separate large-diameter BaF_2:Y ingots.

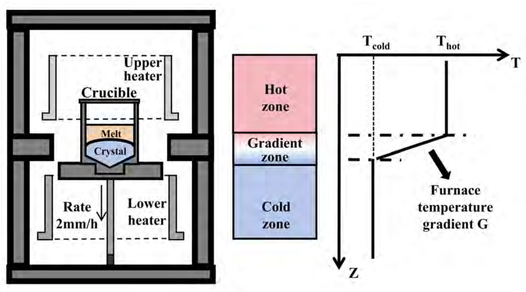
➢ In the first study, measured thermophysical properties and thermal-stress analysis were used to define allowable growth and cooling conditions for BaF_2 with Y doping concentration up to 15 at.%. An axial temperature gradient of 9 °C·cm^{-1} and a temperature-dependent segmented cooling schedule enabled the crack-free growth of a 4-inch-diameter, 8-cm-long crystal. The crystal maintained high visible-range transmittance over most of the measured region, although the tail-end optical quality requires further improvement. In the second study, transverse light-response uniformity was investigated using 10 × 10 × 55 mm^3 bars cut from an ingot with a nominal Y concentration of 10 at.%. LA-ICP-MS showed no measurable macroscopic radial Y gradient within the selected region, yet dual-ended measurements revealed a clear position dependence in the collected response. Quotient analysis showed limited light-yield-related asymmetry and substantially larger transport-related asymmetry. Measurements under different wrapping conditions established sensitivity to the optical boundary. Under the fixed inputs used in optical-only Geant4 simulations, surface and interface losses exceeded bulk absorption.

➢ Together, these results connect thermal-field control, composition assessment and optical-boundary engineering in the development of large BaF_2:Y scintillators with controlled detector response. Future work will validate the spatial and temporal response of longer crystals using controlled optical packaging and detector-representative readout conditions.

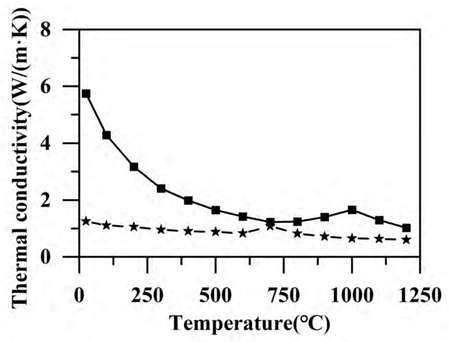
Keywords BaF_2:Y scintillator, large-diameter crystal growth, thermal-stress control, light-response uniformity, light transport loss, fast radiation detection

1.Growth and optical quality

15 at.% Y: three-zone vertical Bridgman growth. Thermophysical measurements inform stress control and segmented cooling. [1]



(a) Three-zone vertical Bridgman growth configuration.



(b) 15 at.%Y doping changes the thermal-conductivity balance

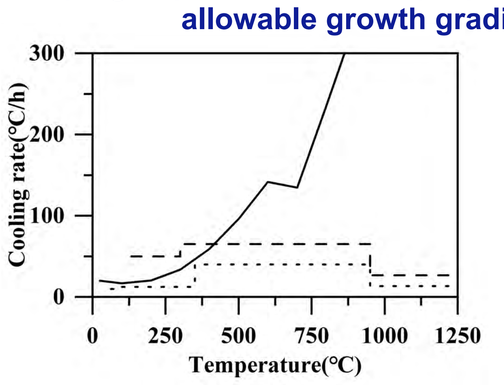
Maximum acceptable axial temperature gradient

$$G_{max}\left(\frac{dT}{dz}\right)_{max} = \frac{4\varepsilon_b}{\alpha R^{3/2}}\frac{1}{\sqrt{h}}\left(1-\frac{1}{2}\mathrm{hR}\right) \propto R^{-3/2}$$

the Maximum cooling rate:

$$V_{max} = \left[\frac{dT}{dt}\right]_{max} = \frac{8^{1/2}\kappa\varepsilon_b}{c\alpha R^2} \propto R^{-2}$$

Doping-dependent thermal properties provide the basis for defining allowable growth gradients and cooling rates.



(c) Segmented cooling kept the schedule below V_{max}

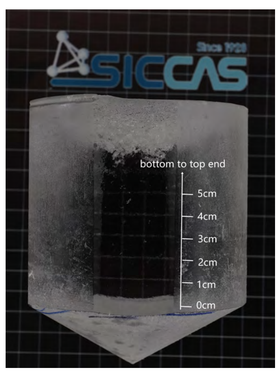


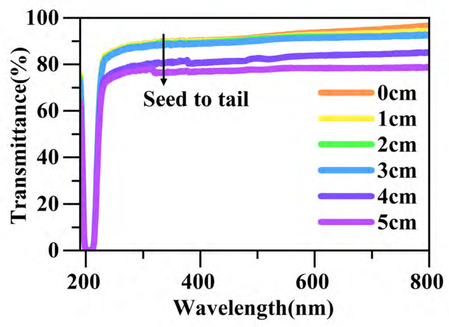
(d) Cracking remains before cooling control



(e) Crack-free 4-inch crystal after optimization

Gradient control and slower low-temperature cooling work together to enable crack-free growth.



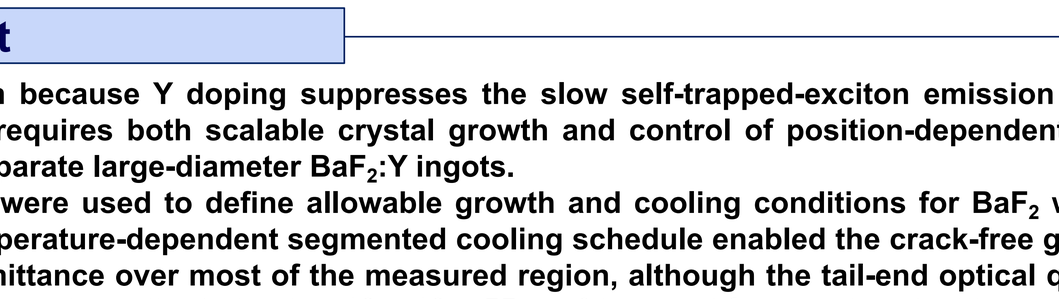


Double-side-polished crystal and radial transmittance spectra measured at successive axial positions over a 96-mm optical path.

Axial transmission differences identify optical-quality refinement as the next growth challenge after crack suppression.

2.Composition and light transport

Separate nominal 10 at.% Y ingot: eight 55-mm radial bars. LRU uses reversible single-end PMT readout. [2]

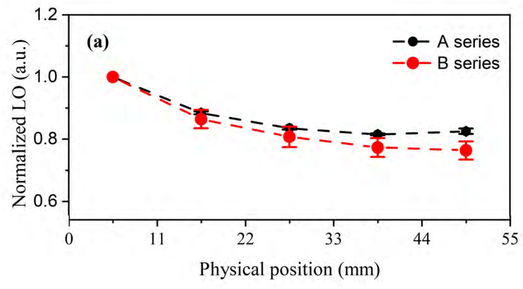


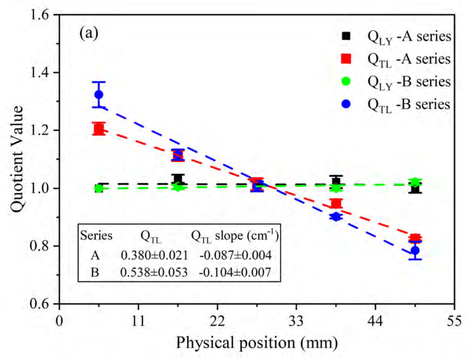
(h,i) Radial sampling geometry and LA-ICP-MS mapping of the $^{89}Y/^{132}Ba$ signal ratio in a representative wafer.

Limited macroscopic radial Y variation provides a composition baseline for examining the remaining response nonuniformity.

$S_L(i) = A_iB_i$ $\quad$ Q_{LY} —— yield symmetry $Q_{LY}(i) = S_L(i)/S_R(i) = A_i/A_{n+1-i}$

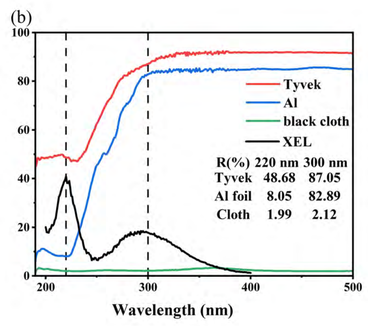
$S_R(i) = A_{n+1-i}B_i$ $\quad$ Q_{TL} ——transport symmetry $Q_{TL}(i) = S_L(i)/S_R(n+1-i) = B_i/B_{n+1-i}$



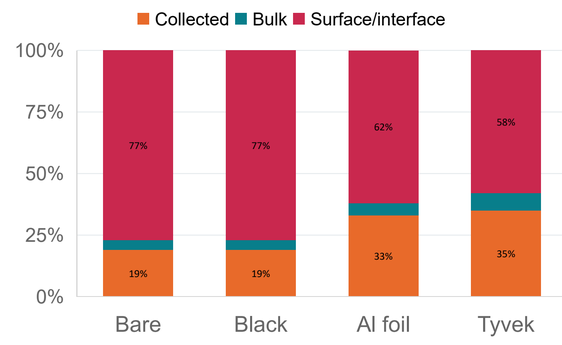


(j,k) Normalized light-response profiles and yield-related Q_{LY} and transport-related Q_{TL} quotients for the two radial sample series.

Near-unity Q_{LY} and strongerQ_{TL} variation favor a transport-related interpretation under the symmetry assumptions.



(l) Deep-UV Wrapping reflectance across the BaF_2:Y emission bands.



(m) simulated photon-loss fractions at the bar centre under fixed optical inputs.

The wrapping experiment establishes boundary sensitivity; the optical model identifies surface and interface losses as a candidate explanation.

Summary and Outlook

Summary

Large-diameter growth establishes the material platform; radial diagnostics identify optical transport as a further optimization target.

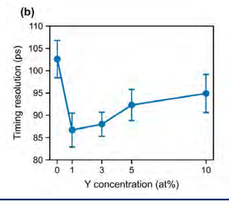
Growth control: Thermophysical analysis guided the axial gradient and segmented cooling strategy, enabling crack-free growth of a 4-inch BaF_2:15 at.%Y crystal. Further refinement is needed to reduce inclusions and improve ultraviolet optical quality.

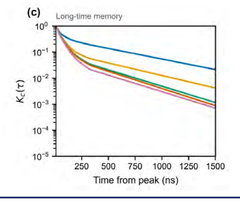
Response diagnostics: With limited radial Y variation in the sampled region, quotient analysis indicates that the observed response nonuniformity is more consistent with optical transport than with large intrinsic light-yield variation.

Optimization direction: The same-crystal wrapping test confirms boundary sensitivity. Surface finish, wrapping and readout coupling should therefore be optimized alongside crystal growth and composition uniformity.

Outlook

Future work will determine how growth quality and optical packaging jointly affect spatial and temporal response in longer BaF_2:Y crystals. Position-resolved waveform measurements will assess light collection, prompt timing and post-event persistence within the same detector configuration. Driven measurements will then test where predictions based on isolated-event responses remain valid and where rate-dependent effects require additional modeling.





Prompt timing and post-event persistence describe different aspects of detector response and require separate assessment.

Measured isolated-event timing resolution and reconstructed detector-response tails for a separate 0–10 at.% Y concentration series.

Supported in part by the Strategic Priority Research Program of the Chinese Academy of Sciences under Grant XDA25030600; in part by the National Key Research and Development Program of China under Grant 2022YFB3503902, also in part by the National Natural Science Foundation of China under Grand U2541244, and in part by the Opening Fund of the Key Laboratory of Rare Earths, Chinese Academy of Sciences.

[1] J. Zhang et al., J. Crystal Growth 677 (2026) 128460.
[2] J. Zhang et al., RDTM, under review.

[C10]

Development of a TES-Based Hard X-Ray Spectrometer

Haoyu Li[1],[2], Daikang Yan[1],[2],*

[1] Institute of High Energy Physics, Chinese Academy of Sciences, Beijing 100049, China
[2] University of Chinese Academy of Sciences, Beijing 100049, China Corresponding author: yandk@ihep.ac.cn

Abstract

Conventional semiconductor-based energy-dispersive spectrometers offer high detection efficiency but relatively limited energy resolution, whereas crystal-based wavelength-dispersive spectrometers can achieve excellent energy resolution at the cost of collection efficiency and simultaneous spectral coverage. Transition-edge sensor (TES) microcalorimeters can combine high energy resolution, high detection efficiency, and broadband spectroscopic capability.

This work describes the development of a TES-based hard X-ray spectrometer, including aluminum–manganese (AlMn) TES design, absorber optimization, electrothermal characterization, and system-level design and simulation. The spectrometer targets an energy resolving power of E/ΔE ~ 2000 over the 10–100 keV energy range. TES devices exploit the steep resistance–temperature dependence within the superconducting transition to resolve the small temperature rise produced by an absorbed photon. The transition temperature (Tc) of AlMn films can be adjusted by annealing, which facilitates control of Tc and its uniformity across detector arrays. A gold–bismuth bilayer absorber is used to combine the high thermal conductivity of gold with the relatively low heat capacity and high X-ray stopping power of bismuth. The absorber geometry and TES–absorber coupling are optimized for efficient thermalization while reducing position-dependent response and maintaining a balance between energy resolution and absorption efficiency. Electrothermal measurements are used to characterize device performance and guide further detector optimization and cryogenic system integration.

The development can be used for applications in hard X-ray Compton spectroscopy and X-ray emission spectroscopy at synchrotron radiation facilities. The TES detector can also be used for 511-keV positron-annihilation spectroscopy of the Galactic center.

Keywords: Transition-edge sensor (TES); Hard X-ray spectroscopy

1. AlMn TES Design & Absorber Optimization

10–100 keV	E/ΔE ≈ 2000	Tc ≈ 100 mK	2 μm Au / 5+ μm Bi
Target energy range	Resolving power	AlMn target Tc	Bilayer absorber

1.1 Operating Principle & Negative Electrothermal Feedback

- Photon absorption gives a temperature rise, ΔT = Eγ/C, across the steep R–T transition.
- Voltage bias stabilizes the operating point and speeds up pulse recovery.
- High transition sensitivity, low heat capacity and ≈100 mK operation support high energy resolution.

α = (T₀/R₀)(dR/dT) β = (I₀/R₀)(dR/dI)

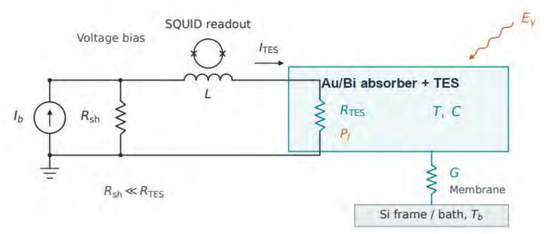


Fig. 1. Voltage-biased TES electrothermal feedback circuit.

$$\Delta E_{\mathrm{FWHM}} = 2\sqrt{2\ln 2}\,\sqrt{\frac{4k_B T_0^2 C}{\alpha}}\sqrt{\frac{n(1+2\beta)}{2}}$$

1.2 AlMn Tc Tuning by Annealing

- AlMn: 200 nm film with 2000 ppm Mn and low magnetic sensitivity.
- Baking at 210 °C gives Tc ≈107 mK.

1.3 Interdigitated Nb Electrodes

Interdigitated electrodes reduce Rn from 50 to 10 mΩ/□.



1.4 Au/Bi Bilayer Absorber & Thermalization

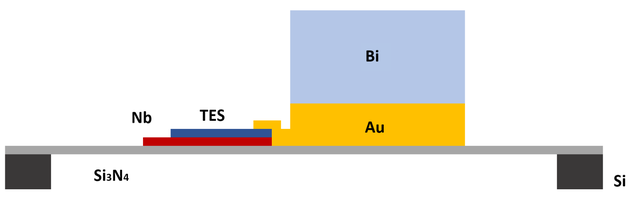


Fig. 2. Original Au/Bi absorber and TES schematic.

- Au (2 μm): Spreads heat and couples the absorber to the TES.
- **Electroplated Bi (5+ μm)**: High stopping power and low heat capacity. Large grains reduce energy trapping.
- Suspended SiN: Sets the weak thermal link to the bath.

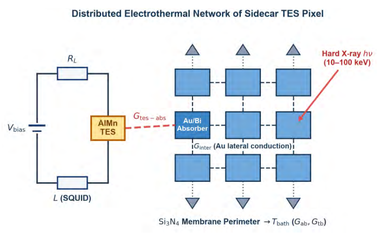


Fig. 3. Distributed FEM thermal network.

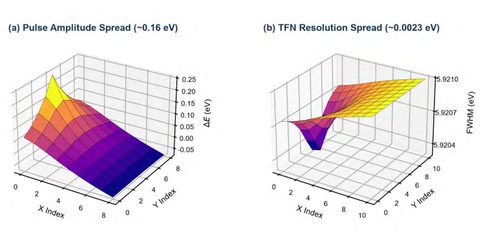
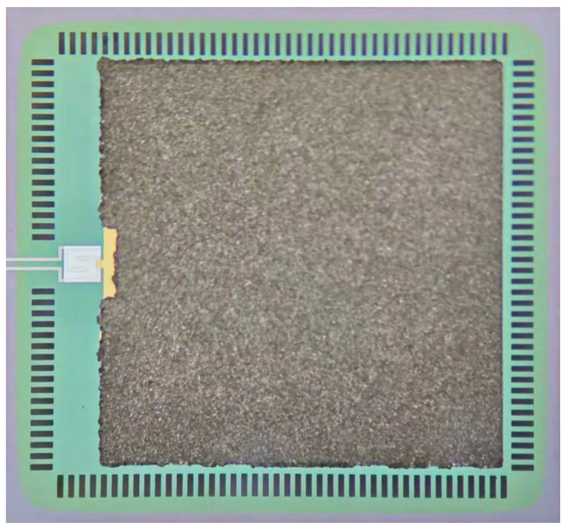
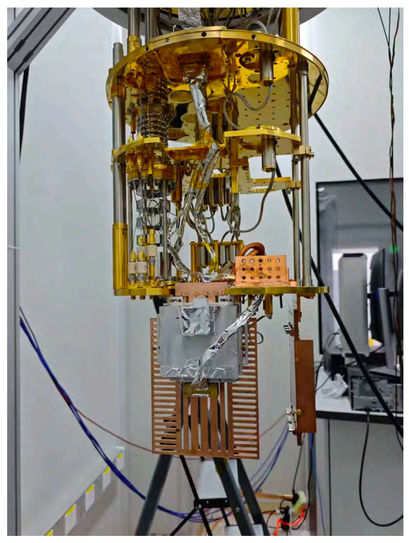


Fig. 4. Modeled position broadening (<0.2 eV).

1.5 TES Device & Cryogenic Setup



TES device



DR cryogenic setup

2. Electrothermal Characterization & X-Ray Calibration

Tests use DR and SQUID readout. I–V, bias-step, complex impedance, noise and X-ray response guide detector optimization.

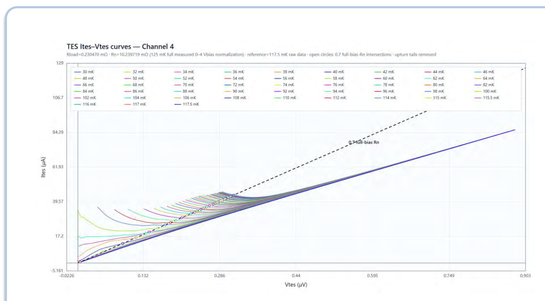


Fig. 5. I–V curves across bath temperature.

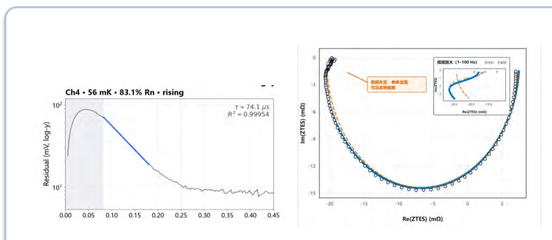


Fig. 6. Bias-step decay and complex Z(f).

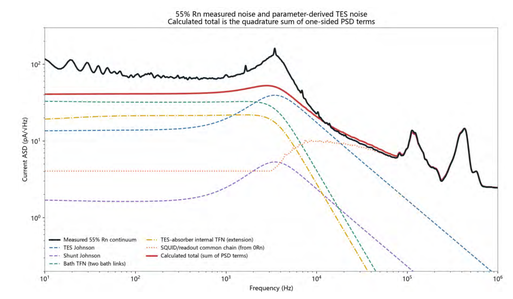


Fig. 7. Current noise ASD.

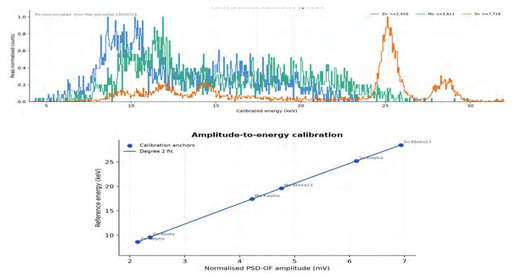


Fig. 8. X-ray spectrum and energy calibration.

Conclusions

A. Calibration linearity deviation is <1%.
B. Electrothermal analysis suggests that an AlMn oxide layer weakens thermal contact, causing photon energy loss from the absorber and poor resolution. The next run will remove this layer during absorber fabrication.

3. Hard X-Ray Compton & Emission Spectrometer

Synchrotron XCS and XES combine high energy resolution with large collection solid angle. The Compton scattering angle is 135°.

$$\Delta p_z = \sqrt{\left(\frac{\partial p_z}{\partial E_1}\Delta E_1\right)^2 + \left(\frac{\partial p_z}{\partial E_2}\Delta E_2\right)^2 + \left(\frac{\partial p_z}{\partial \phi}\Delta\phi\right)^2} \approx 0.17 \text{ a. u.}$$

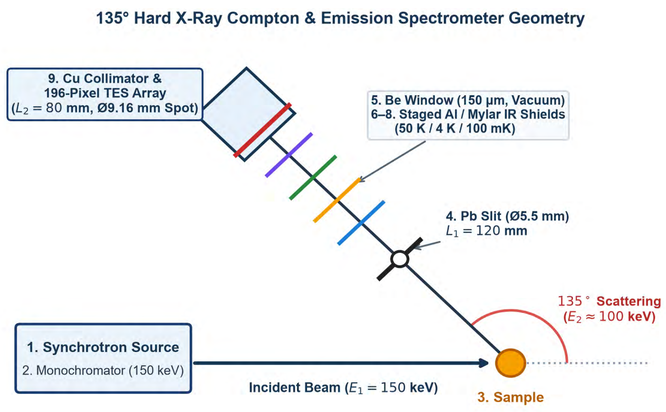


Fig. 9. 135° Compton geometry and IR shields.

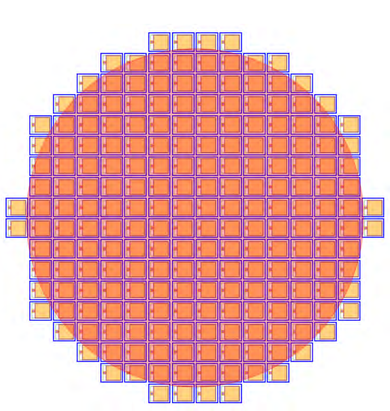


Fig. 10. 196-pixel TES array.

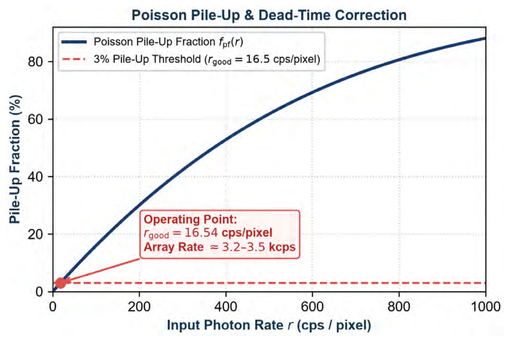


Fig. 11. Pile-up and throughput model.

Key Design Parameters

- E/ΔE ≈2000 at 10–100 keV.
- ΔE ≈50 eV at 100 keV.
- Momentum resolution ≈0.17 a.u.
- 196 pixels; 400 × 400 μm² absorbers.
- 2 μm Au + 5+ μm Bi.
- >3000 counts/s at 3% pile-up (model).

[1] L. Gottardi & K. Nagayoshi. Applied Sciences 11, 3793 (2021).
[2] E. M. Vavagiakis et al. J. Low Temp. Phys. 199, 408–415 (2020).
[3] D. Yan et al. IEEE Trans. Appl. Supercond. 29(5), 1–4 (2019).
[4] F. Shirazi et al. J. Astron. Telesc. Instrum. Syst. 9, 024006 (2023).

CEPC WORKSHOP 2026 C11

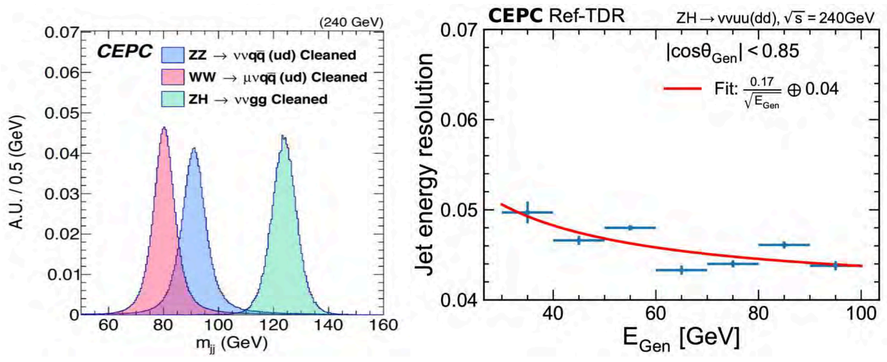
Improved Jet Energy Reconstruction with XGBoost for the CEPC

Yujie Xiong, Haijun Yang, Chunxiang Zhu, Yifan Zhu

Shanghai Jiao Tong University

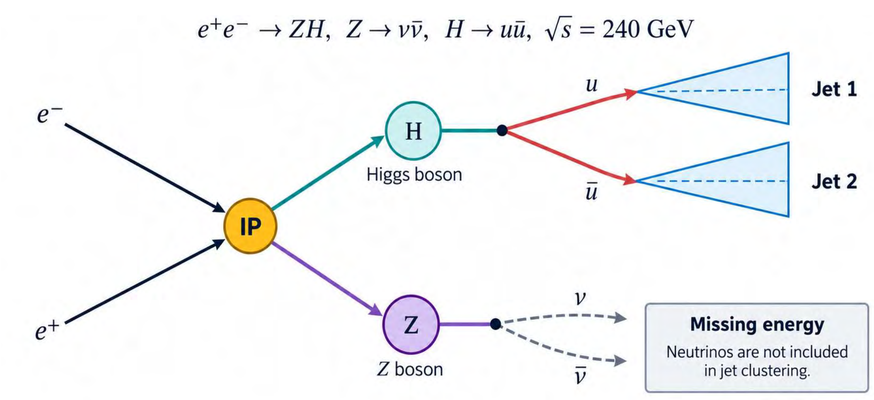
Physics Goal

- Separating hadronic W, Z, Higgs decays motivates jet-energy resolution of **~3-4% at 100 GeV**
- CEPC Ref-TDR reports light-quark JER of 4.5% and $H \to gg$ BMR of 3.87%



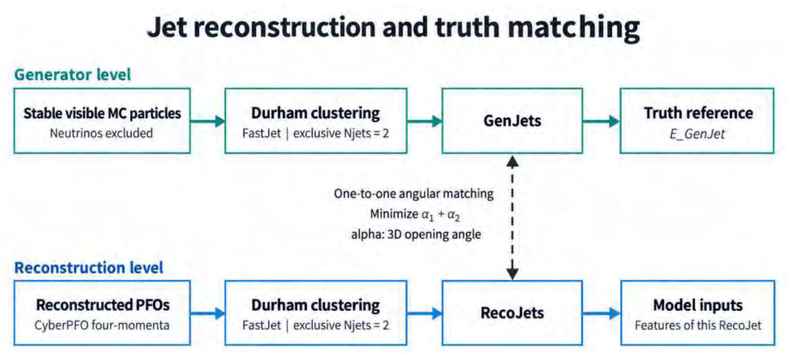
Sample

- Process: $e^+e^- \to ZH \to \nu\bar{\nu}u\bar{u}$, at $\sqrt{s} = 240$ GeV
- Simulation and Reconstruction: CEPCSW 25.3.7
- Nominal Sample: 1M events, 2M jets before selection
- Input: Reconstructed CyberPFO objects, detector info and truth particle



Jet Reconstruction and Selection

- **RecoJet**: cluster CyberPFO four-momenta
- **GenJets**: stable truth particles, excluding υ
- Both collections use **FastJet exclusive $e^+e^-k_t$ clustering (Durham)** with $N_{jets} = 2$
- **RecoJets and GenJets** are matched one-to-one by minimizing the **sum of their opening angles**



- **Energy range:** $30 \leq E_{GenJet} < 100$ GeV
- **Barrel acceptance:** $|cos\theta_{GenJet}| < 0.85$
- **Matching requirement:** $\alpha < 0.2$ rad

60% train / 20% validation / 20% test

The split is performed by source files, keeping jets from the same event in the same dataset. All compared methods use the same selected test jets

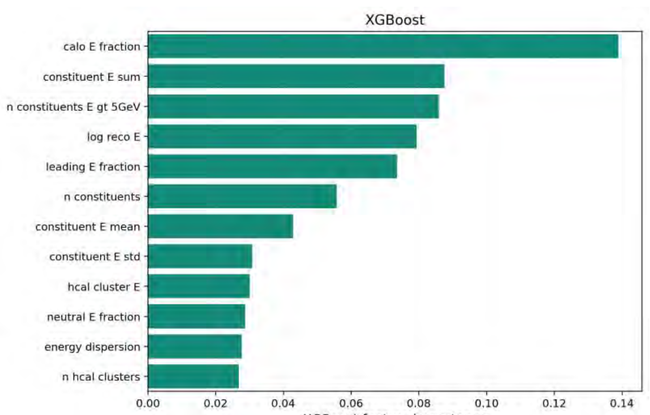
XGBoost

Reconstructed Jet Variables	No of Variables
Jet kinematics	7
Multiplicities and charge	11
Constituent energy distribution	8
Energy composition	4
Calorimeter information	6
Angular shape	7

- Regression function comparison

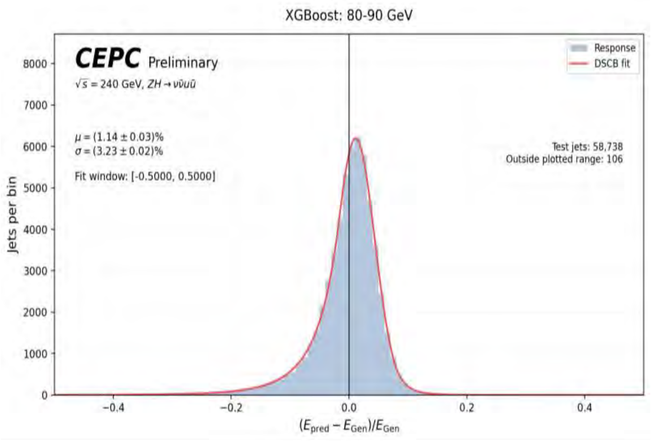
Regression Function	RMSE [GeV]	Mean bias [%]
$ln(E_{GenJet}/E_{RecoJet})$	**4.54**	**0.19**
$E_{GenJet}/E_{RecoJet}$	4.57	0.39
$E_{GenJet} - E_{RecoJet}$	4.52	0.38

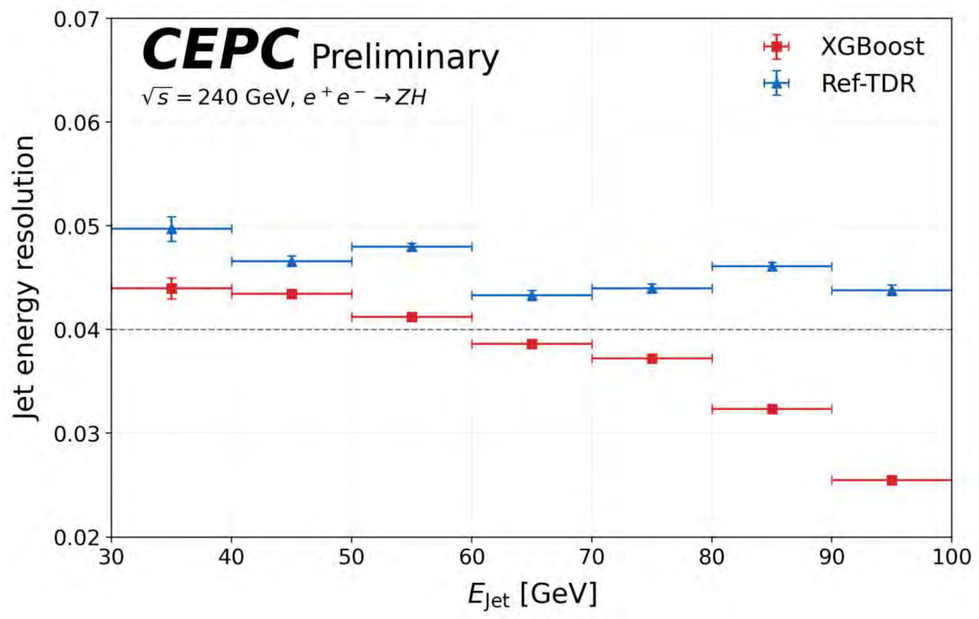
- Importance of input variables



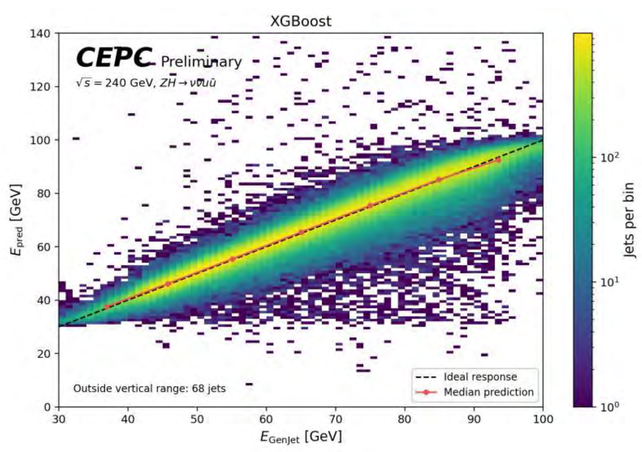
Jet Energy Resolution

- 80-90 GeV Result

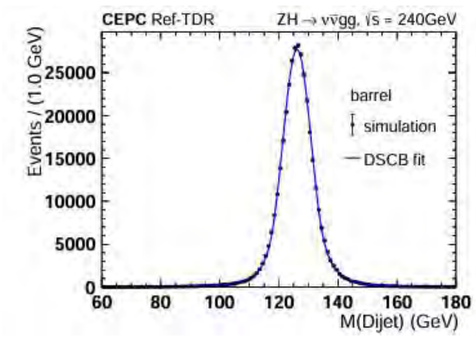


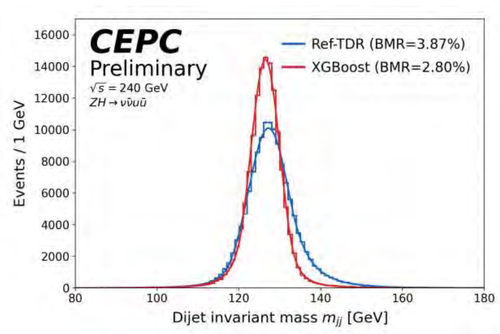


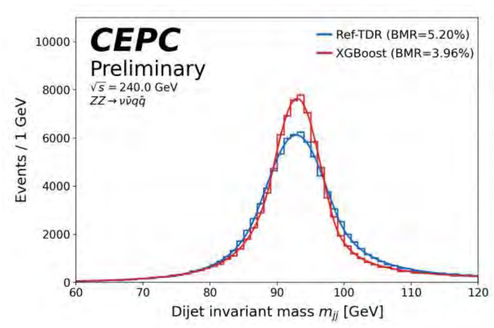
- **JER (Ref-TDR → XGBoost):**
  4.5% → 3.0% (improvement 33%)
- **JER (XGBoost) reaches**
  2.6% at 90-100 GeV

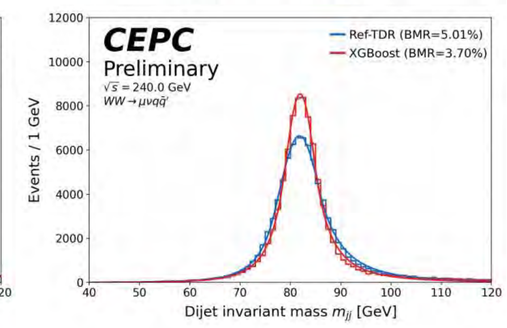


Boson Mass Resolution



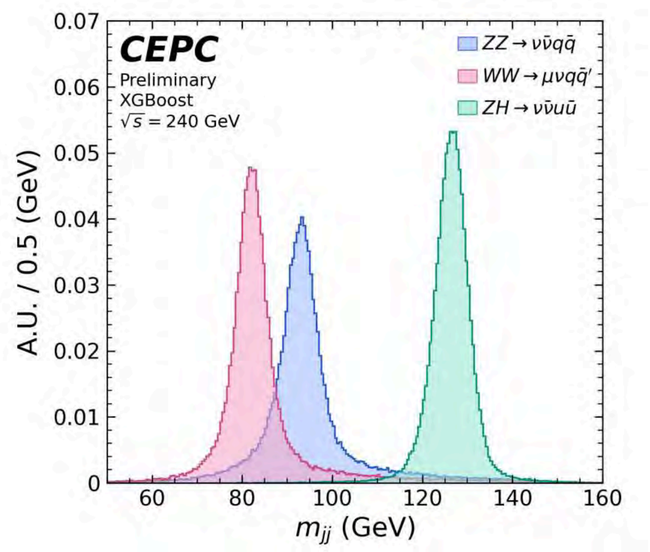






- The XGBoost model trained on $H \to u\bar{u}$ improves dijet mass resolution for all three bosons, without retraining.
- $BMR = \sigma_{core}/\mu$

BMR	Ref-TDR	XGBoost	Improvement
H	3.87%	**2.80%**	**27.6%**
W	5.01%	**3.70%**	**26.1%**
Z	5.20%	**3.96%**	**24.0%**



Conclusions and outlook

- XGBoost significantly improves JER and BMR of Higgs, Z and W by 20-30%
- Next: extend to other Higgs, W and Z decay flavours and estimate its physics impact

[1] CEPC Study Group, CEPC Technical Design Report: Reference Detector (2025), arXiv:2510.05260, Sec. 15.1.7.

C12

The 2026 International Workshop on the
High-Energy Circular Electron-Positron Collider (CEPC2026)

Surface and Bulk Defect Control of $CsPbBr_3$ Single Crystals for Gamma-Ray Spectroscopy

Jie Ma[1], Junqiang Wang[2], Kelin Shen[1], Shaohan Wang[1], Run Xu[2*], Junfeng Chen[1*]

[1] State Key Laboratory of Functional Crystals and Devices, Shanghai Institute of Ceramics, Chinese Academy of Sciences, Shanghai 200050, China. E-mail: jfchen@mail.sic.ac.cn

[2] School of Materials Science and Engineering, Shanghai University, Shanghai 200444, China. E-mail: runxu@shu.edu.cn

Introduction

- $CsPbBr_3$ single crystals combine strong X/γ-ray absorption with favorable carrier transport and room-temperature operation, making them promising semiconductor spectrometers [1,2]. High-resolution γ-ray measurements require efficient charge collection and low electronic noise [2,3].
- Crystal growth and detector fabrication inevitably introduce bulk impurities and surface damage into $CsPbBr_3$ single crystals, yet their effects on carrier transport and γ-ray detection remain insufficiently understood. This work investigates bulk impurity control and surface-state engineering to address these limitations.

Surface defect control

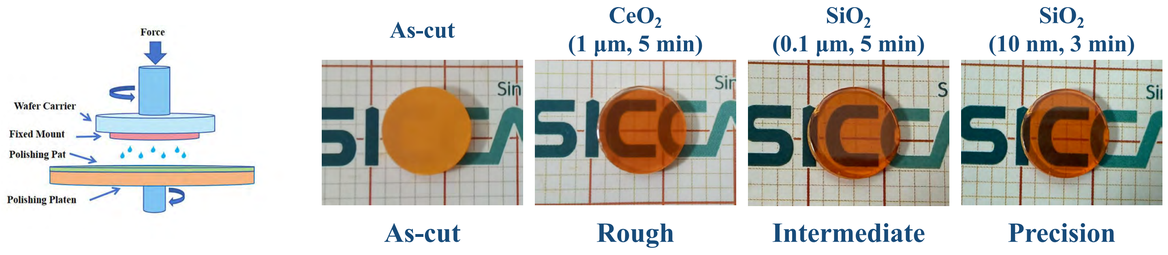


Figure 1. Polishing setup and evolution of the crystal surface

➢ Controlled polishing conditions (abrasive material and particle size, polishing time, pressure and rotation speed) yielded distinct surface states and defined the optimal processing window.

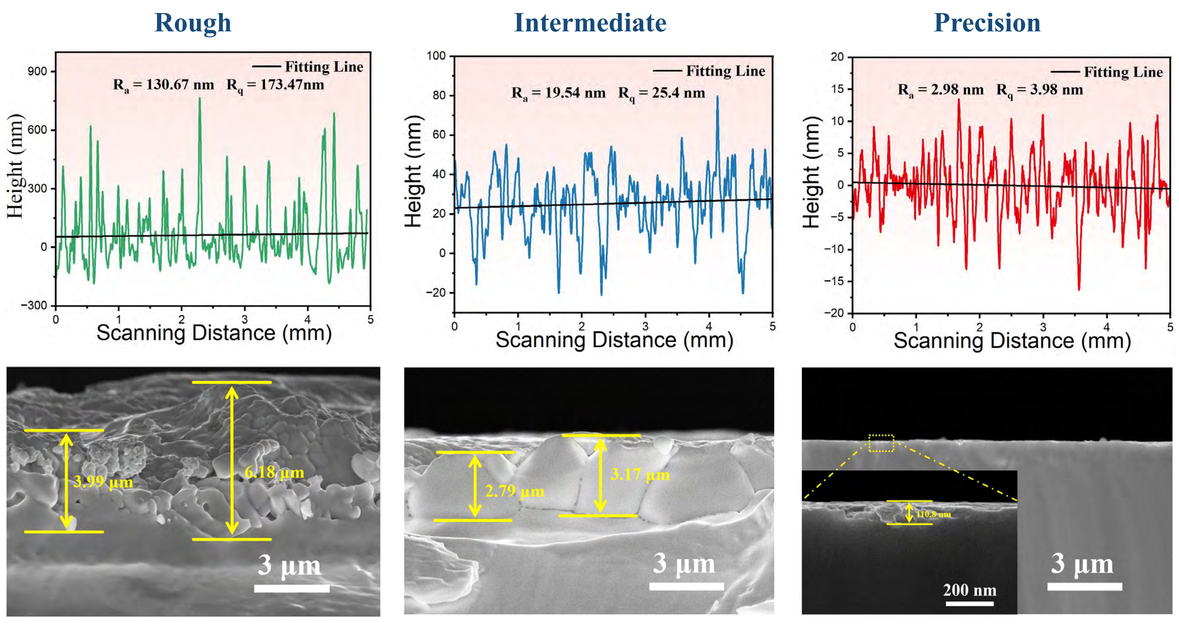


Figure 2. Surface profiles and cross-sectional damage after sequential polishing

➢ From intermediate to precision polishing, profilometric roughness decreases from 19.54 to 2.98 nm and the damage layer thins from about 3 μm to 110 nm.

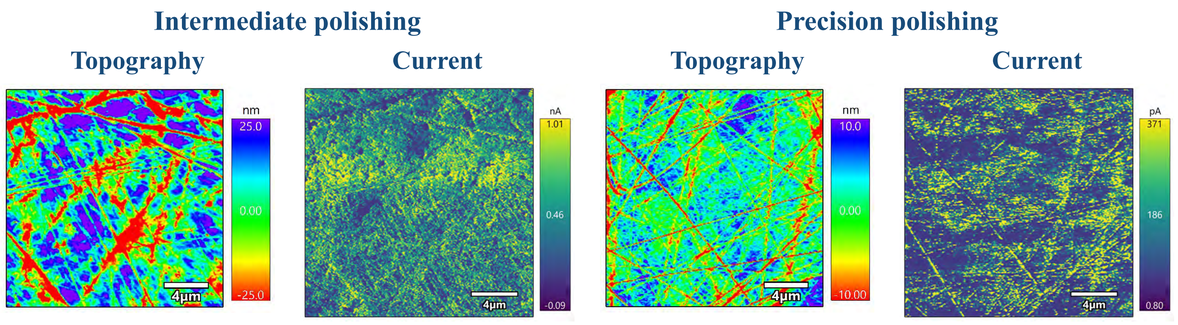


Figure 3. C-AFM topography and current maps at different surface states.

➢ Fewer scratches and local leakage paths accompany the reduced C-AFM current (from 338.1 to 141.2 pA), and the dark current decreases from 210 to 30.3 nA at 200 V.

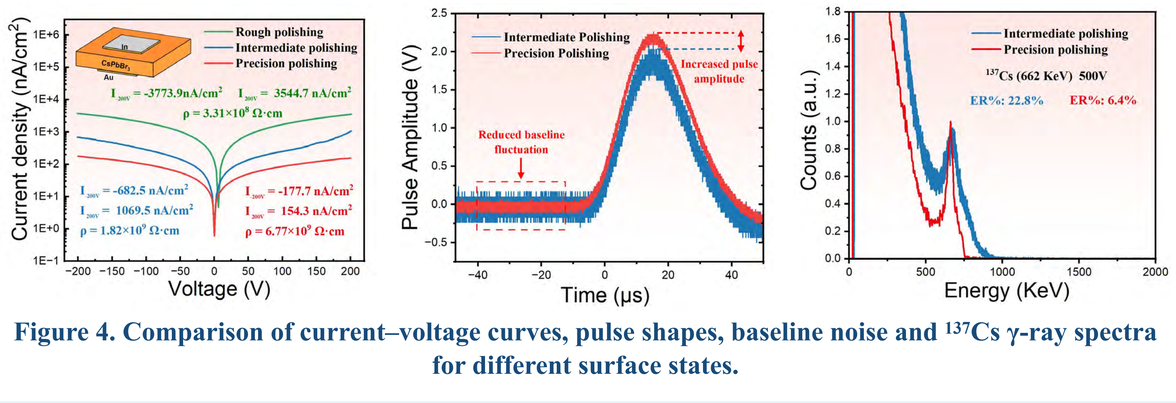


Figure 4. Comparison of current–voltage curves, pulse shapes, baseline noise and ^{137}Cs γ-ray spectra for different surface states.

➢ For the same detector under matched test conditions, energy resolution improves from 22.8% to 6.4% for ^{137}Cs 662 keV γ-rays at 500 V, consistent with higher resistivity and lower electronic noise.

Bulk impurity control

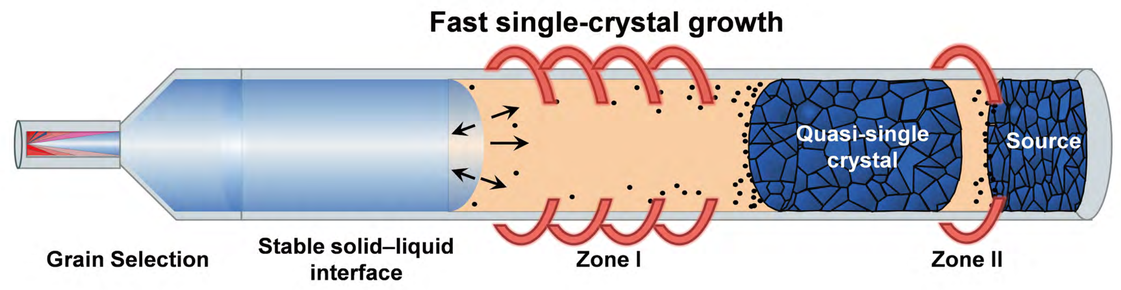


Figure 5. Dual-zone iterative refining and simultaneous crystal growth

➢ Iterative horizontal zone refining couples in situ purification with directional recrystallization to yield intact $CsPbBr_3$ single crystals at 25mm/h , a 25-fold increase over the Bridgman reference rate.

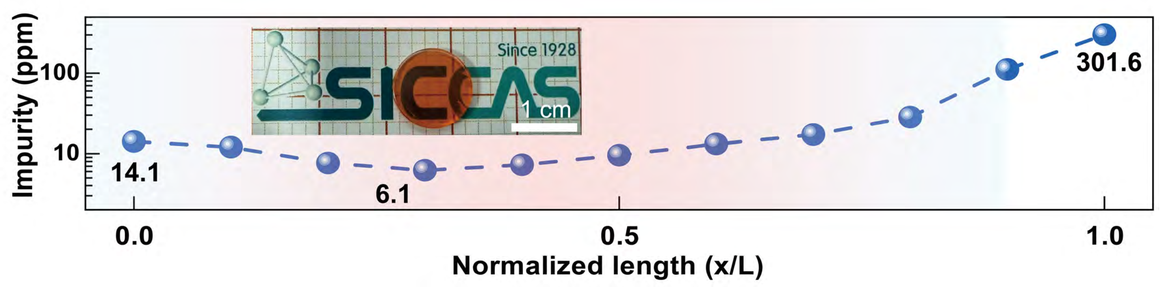


Figure 6. Axial variation in total impurity concentration

➢ Glow discharge mass spectrometry (GDMS) finds a minimum total impurity concentration of 6.1 ppm in the middle region.

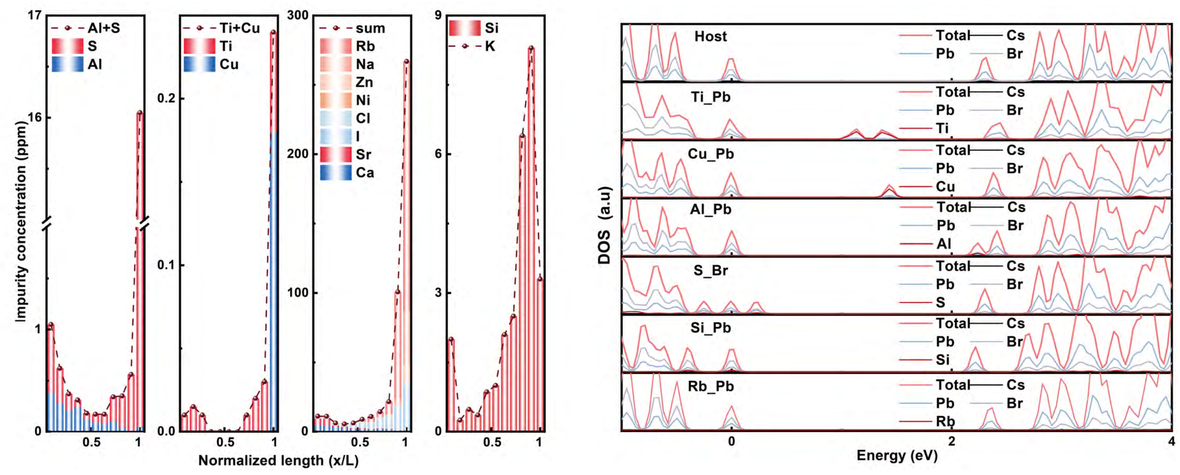


Figure 7. Axial elemental distributions and calculated densities of states

➢ GDMS analysis and DFT calculations revel that zone refining suppresses Cu- and Ti-related deep-level trapping, thereby improving charge transport.

Figures 8. Axial carrier transport, optimum γ-ray spectra, and energy resolution versus growth rate.

➢ Crystals from the middle region exhibit $\mu\tau = 1.2 \times 10^{-3}$ cm^2 V^{-1}, and the corresponding planar detectors achieve a best energy resolution of 3.4%.

Conclusions and Outlook

- **Surface optimization reduces conductive pathways and improves electrical performance, suppressing electronic noise and ultimately improving the signal-to-noise ratio and energy resolution.**
- **Iterative dynamic zone refining with synchronized dual-zone scanning directly yields high-quality $CsPbBr_3$ single crystals with low impurity concentrations.**
- **Bulk impurity control improves carrier transport, while surface damage removal suppresses leakage. Their combination could further enhance $CsPbBr_3$ γ-ray detector performance.**

References

[1] C. C. Stoumpos et al. Crystal growth of the perovskite semiconductor $CsPbBr_3$: a new material for high-energy radiation detection. *Cryst. Growth Des.* 13, 2722–2727 (2013). DOI: 10.1021/cg400645t.

[2] Y. He et al. High spectral resolution of gamma-rays at room temperature by perovskite $CsPbBr_3$ single crystals. *Nat. Commun.* 9, 1609 (2018). DOI: 10.1038/s41467-018-04073-3.

[3] Y. He et al. $CsPbBr_3$ perovskite detectors with 1.4% energy resolution for high-energy γ-rays. *Nat. Photonics* 15, 36–42 (2021). DOI: 10.1038/s41566-020-00727-1.

[4] J. Ma et al. Surface-state-dependent performance of $CsPbBr_3$ perovskite single crystals: from defect suppression to energy resolution enhancement. *J. Mater. Chem. C* (2026). DOI: 10.1039/d6tc01662f.

CEPC 2026, Shanghai, China, Oct 2026
The 2026 International Workshop on the High Energy Circular Electron Positron Collider

C13

Scintillation and Radiation Damage Performance of Yttrium Doped BaF_2 Crystals

Jiawei Xu[1,2], Xiang Li[1], Jing Zhang[1,2], Mingxue Deng[1,2], Jiansheng Xie[1], Xuejun Qi[1], Junfeng Chen[1,2*]

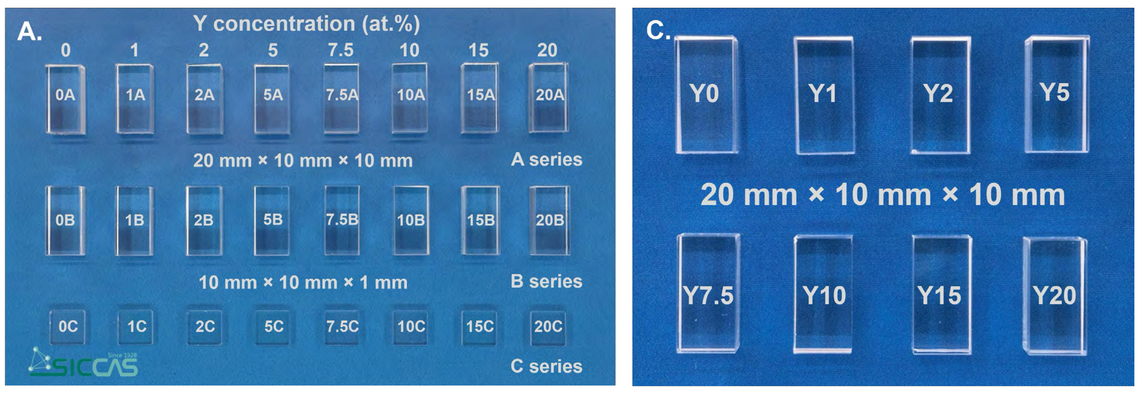
1. State Key Laboratory of Functional Crystals and Devices, Shanghai Institute of Ceramics, Chinese Academy of Sciences, Shanghai 201899, China
2. Center of Materials Science and Optoelectronics Engineering, University of Chinese Academy of Sciences, Beijing 100049, China

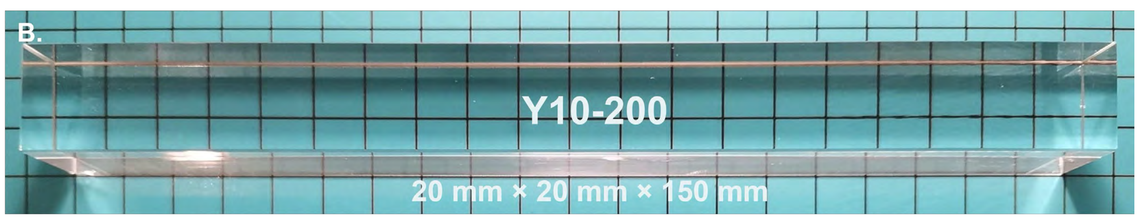
*Corresponding Author Email: jfchen@mail.sic.ac.cn

Introduction

■ **Barium fluoride (BaF_2) is a classic ultrafast scintillator with a sub-nanosecond fast component. Following our group's demonstration that yttrium (Y) doping effectively suppresses its intrinsic slow component [1-2], systematic investigations of the concentration-dependent scintillation performance and radiation tolerance are needed to guide its application in high-energy physics detectors.**

Material Characterization

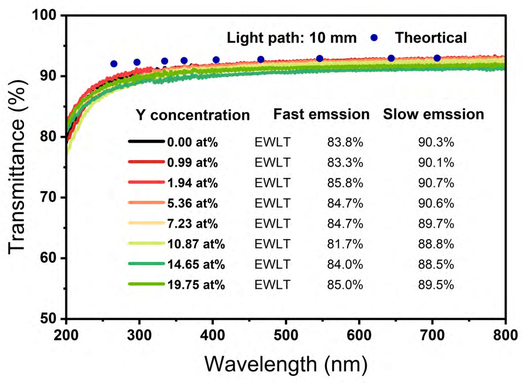


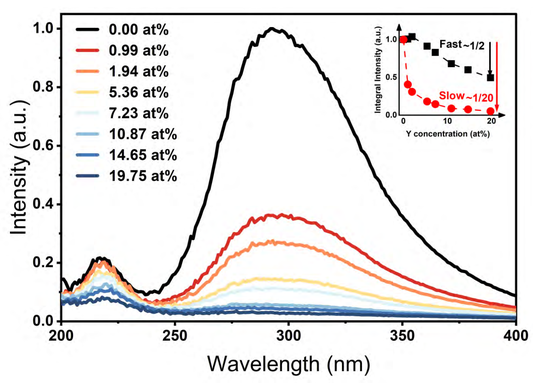


➢ **BaF_2 crystals with nominal Y concentrations of 0–20 at.% were systematically characterized in terms of optical transmittance, radioluminescence, light output (LO), fast-to-slow component ratio (F/S), energy resolution, and decay kinetics. Radiation damage was assessed after γ-ray irradiation at cumulative doses of 10 krad–10 Mrad. A 200-mm-long BaF_2:Y crystal with a nominal Y concentration of 10 at.%, obtained via vertical Bridgman growth, was also characterized to evaluate its optical and scintillation properties and light-response uniformity (LRU).**

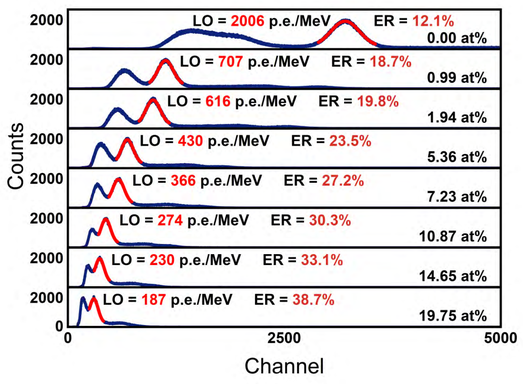
A. Scintillation Performance of BaF_2: Y crystal

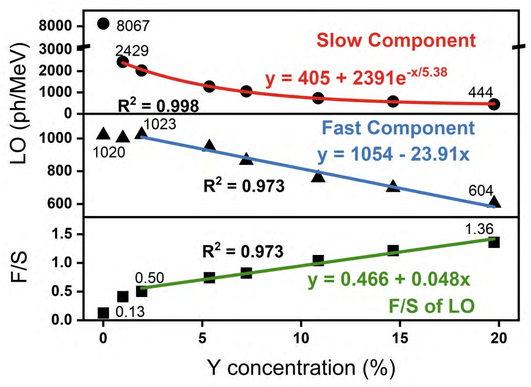
■ **Transmittance and Radioluminescence**



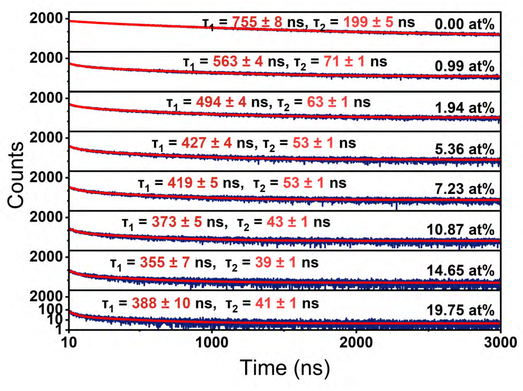


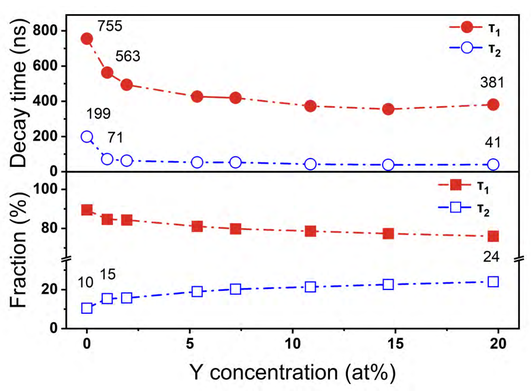
■ **Light Output (LO) and F/S of LO**





■ **Slow Components' Decay Times and relative Fractions**





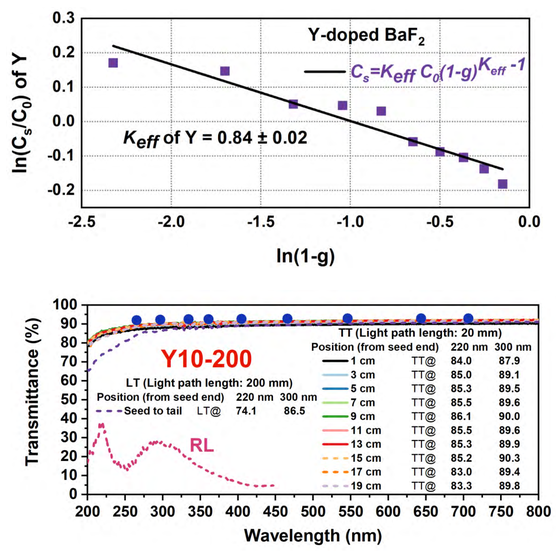
➢ The transmittance of samples showing that Y doping has no significant effect on the optical performances of BaF_2 crystal. Both the slow and fast component intensities evolve in two distinct stages.

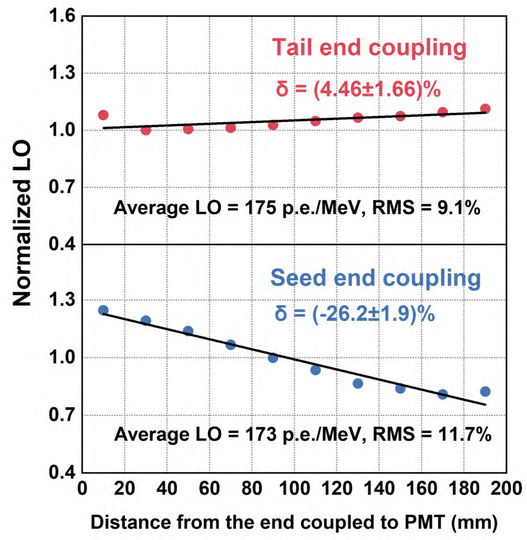
➢ At 20 at.% Y, the fast- and slow-component LOs decreased to 60% and 6% of those of undoped BaF_2, respectively, increasing the F/S ratio from 0.13 to 1.36, while the energy resolution at 511 keV deteriorated from 12.1% to 38.7%.

➢ The two decay times of the slow component shortened from 755 to 381 ns and from 199 to 41 ns with increasing Y concentration.

B. 200-mm-long BaF_2: Y crystal

■ **Segregation, Transmittance and Light Response Uniformity (LRU)**

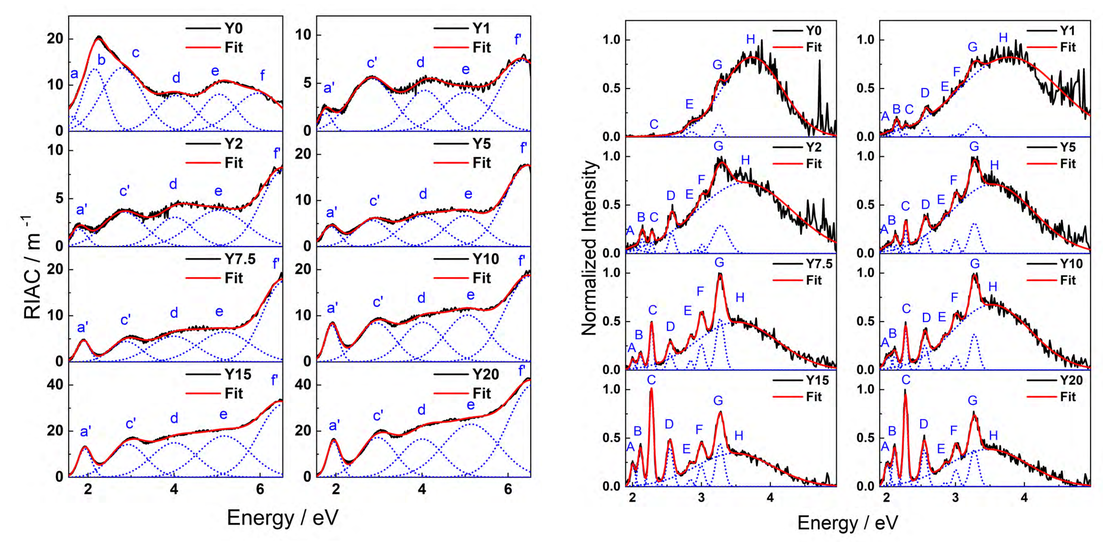




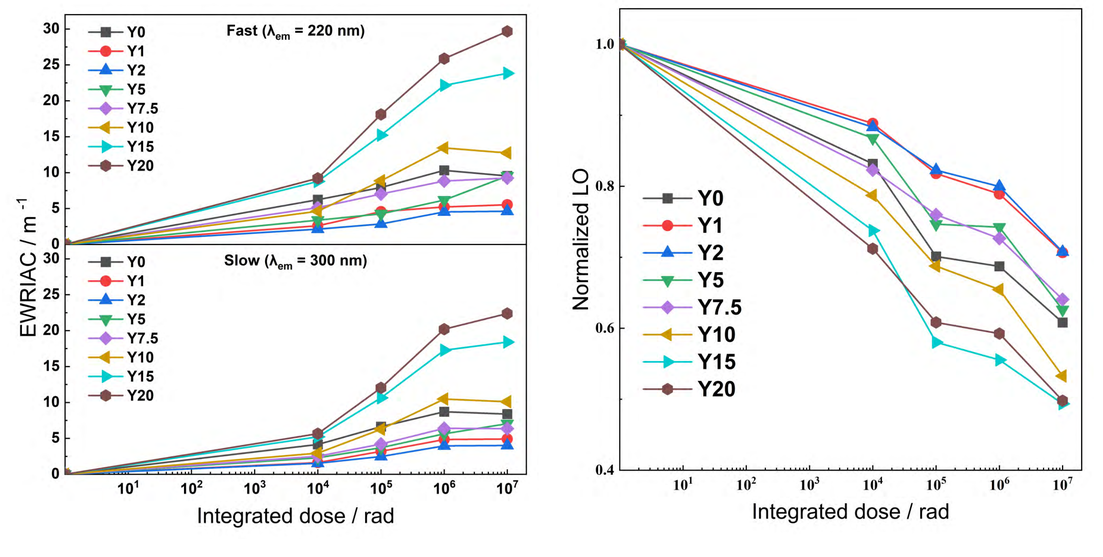
➢ For the 200-mm-long, 10 at.% Y-doped crystal, the effective Y segregation coefficient was 0.84. The crystal exhibited good optical transmittance and LRU, with its slow-component intensity suppressed by approximately one order of magnitude relative to undoped BaF_2.

C. Radiation Damage of BaF_2: Y crystal

■ **Radiation-Induced Absorption and Phosphorescence**



■ **EWRIAC and LO losses**



➢ Y doping causes the broad absorption band in the 400–700 nm (1.77-3.1 eV) range to transform into discrete absorption peaks, with some peaks disappearing and some peaks gradually blue-shifting as the doping concentration increases. Besides the broad band at ~330 nm (3.7 eV) [3], Y-doping induces additional narrow phosphorescence peaks that intensify proportionally with Y concentration.

➢ When the Y concentration reaches 7.5 at.% (with an optimal concentration of 2 at.%), the radiation resistance of BaF_2 is improved. When the Y concentration is ≥10 at.%, the damage level significantly increases compared to undoped BaF_2.

Acknowledgments

➢ National Key Research and Development Program of China (2022YFB3503902); Strategic Priority Research Program of the Chinese Academy of Sciences (XDA25030600).

References

[1] J. Chen, et al., *IEEE Trans. Nucl. Sci.*, vol. 65, no. 8, pp. 2147-2151, 2018.
[2] C. Peng, et al., *IEEE Trans. Nucl. Sci.*, vol. 69, no. 9, pp. 2083-2088, 2022.
[3] C. L. Woody, et al. *IEEE Trans. Nucl. Sci.*, vol. 39, no. 4, pp. 515–523, 1992.

Simulation and Performance Study of a Forward RICH at CEPC

C14

Changru Li[1,2], Shengsen Sun[2], Haojie Dong[2], Jian Wang[2], Zhonghua Qin[2], Yifang Wang[2]

[1]University of Chinese Academy of Sciences (UCAS), Beijing 100049, China | [2]Institute of High Energy Physics (IHEP), CAS, Beijing 100049, China

1. Physics Motivation & Forward PID Challenge

- **CEPC Flavor Physics Goal:** Demands exceptional Particle Identification (PID) with **3σ K/π separation for momentum up to 20 GeV/c**.
- **Forward Region Bottleneck:** Baseline PID (dE/dx or dN/dx + ToF) suffers a severe Kaon ID efficiency drop at p > 3 GeV/c in the forward endcap ($|\cos\theta|$ > 0.88).
- **Forward RICH Placement Options:** Option 1 (0.88 < $|\cos\theta|$ < 0.99, between 3rd & 4th ITK endcap) vs. Option 2 (0.94 < $|\cos\theta|$ < 0.99, outside 4th ITK endcap).

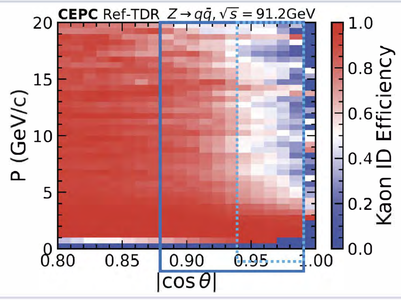


Fig. 1: Baseline Kaon ID efficiency drop in forward region (CEPC Ref-TDR $Z \to q\bar{q}$, $\sqrt{s}$ = 91.2 GeV).

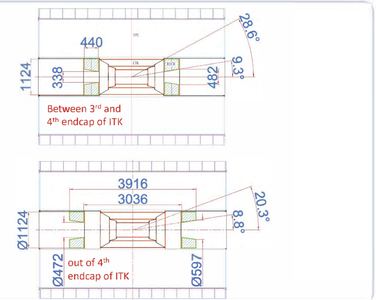


Fig. 2: Candidate locations of Forward RICH inside CEPC tracker volume.

2. CEPCSW Simulation Chain, Geometry & Material Budget

Full Simulation Chain in CEPCSW (Key4hep Stack): DD4hep (detector geometry, materials & optical surfaces) → Geant4 (Cherenkov transport, boundary processes, absorption, Rayleigh scattering) → SiPM Digitization (PDE + Dark Noise) → PID Benchmark.

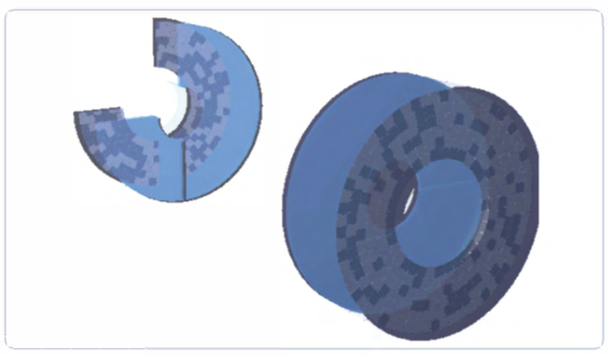


Fig. 3: DD4hep 3D model.

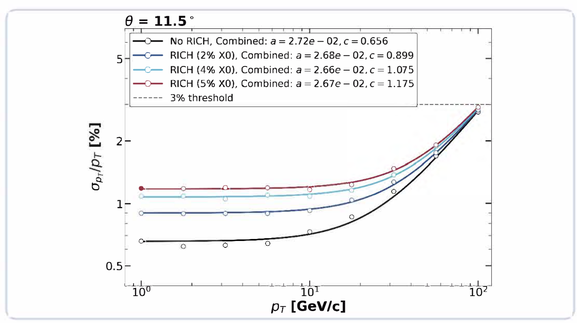


Fig. 4: Impact of RICH material on p_T resolution, still satisfying < 3% requirement.

Component	Material & Thickness	X_0	Budget
Radiator	SiO_2 Aerogel (6 cm)	> 700 cm	< 1% X_0
Photon Det.	SiPM+PCB (1+1 mm)	9.4/19.4cm	1.57% X_0
Shell/Mech.	CF (0.4 mm)+Cu/Ti	40.0 cm	1–3% X_0

Config (θ = 11.5°)	Spatial a	MCS c
No RICH Baseline	2.72e-2	0.656
RICH (2% X_0)	2.68e-2	0.899
RICH (4% X_0)	2.66e-2	1.075
RICH (5% X_0)	2.67e-2	1.175

3. Focusing Aerogel Radiator with Gradient Refractive Index

Increasing radiator thickness l boosts photoelectron yield ($N_{\text{p.e.}} \propto \sin^2\theta_c \cdot l \cdot \Delta E \cdot \epsilon$), but worsens single-photon emission point uncertainty σ_{emission}. Adopting a **3-layer gradient refractive index** (2 cm per layer: **n_1 = 1.007, n_2 = 1.008, n_3 = 1.009**) focuses Cherenkov rings onto the SiPM plane:

$$\sigma_{\theta_c}^{(\text{tot})} = \frac{\sigma_{\theta_c}^{(\text{1pe})}}{\sqrt{N_{\text{p.e.}}}} \quad , \quad (\sigma_{\theta_c}^{(\text{1pe})})^2 = \sigma_{\text{SiPM}}^2 + \sigma_{\text{emission}}^2 + \sigma_{\text{track}}^2 + \sigma_{\text{chromatic}}^2 + \sigma_{\text{rec}}^2$$

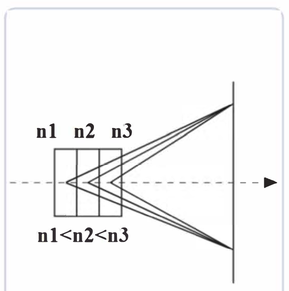


Fig. 5: Focusing principle.

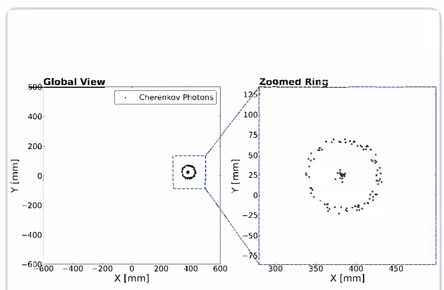


Fig. 6: Unfocused ring (π^-, 10 GeV, θ = 15°).

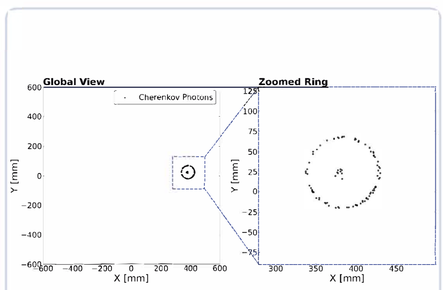


Fig. 7: Focused ring (π^-, 10 GeV, θ = 15°).

4. Optical Processes (Rayleigh, Reflection) & SiPM Digitization

- **Rayleigh Scattering & Mirror Reflection:** $P = 1 - e^{-\Delta s/L_{\text{sc}}}$ with $L_{\text{sc}} = (\lambda/400\ \text{nm})^4 \times 4.6$ cm; outer reflection film reflects high-θ photons, forming folded crescent rings.
- **SiPM Granularity & Hamamatsu MPPC Response:** Requires $\sigma_{\theta_c}^{(\text{tot})} < 0.7$ mrad ⇒ pixel pitch ≤ 1 mm ($\sigma_{\text{SiPM}} = \Delta_{\text{channel}} / (L\sqrt{12})$). Modeled with λ_p = 450 nm, peak PDE = 50% (101 → 22 hits), DCR = 100 kHz/mm^2, time window = 5 ns (A = 0.808 m^2).

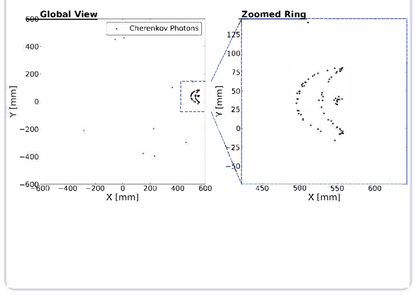


Fig. 8: Ring with Rayleigh & Reflection (π^-, 10 GeV, θ = 22°).

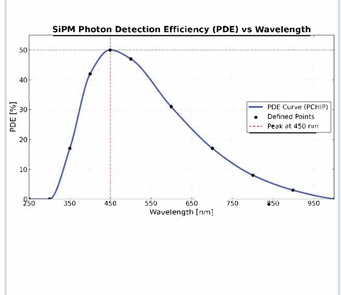


Fig. 9: PDE curve.

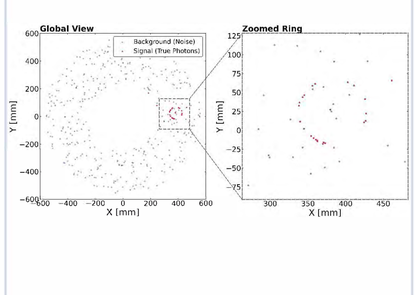


Fig. 10: Ring with PDE + DCR.

5. Cherenkov Ring Reconstruction & K/π Separation Benchmark

3-Step Simplified Reconstruction:

1. **Pre-selection via Circle Fit:** Reject outliers & background hits.
2. **Single-Photon θ_c Calculation:** Geometric ray-tracing from SiPM hit to emission vertex.
3. **Event-Level Aggregation:** Combine clean photoelectrons to evaluate event θ_c and separation power:

$$N_\sigma \approx \frac{|m_K^2 - m_\pi^2|}{2p^2\,\sigma_{\theta_c}^{(\text{tot})}\sqrt{n^2-1}} \quad \Rightarrow N_\sigma = 3.21 > 3 \text{ @ 20 GeV/}c$$

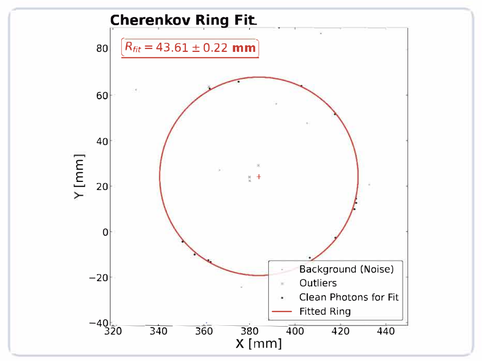


Fig. 11: Circle fit & outlier rejection.

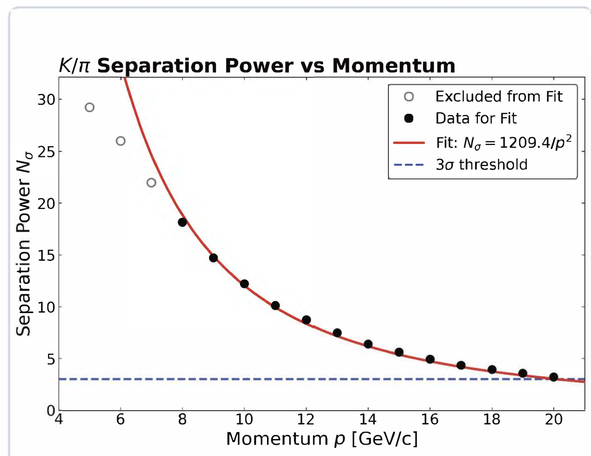


Fig. 12: K/π separation vs. momentum (4–20 GeV/c, θ = 15°).

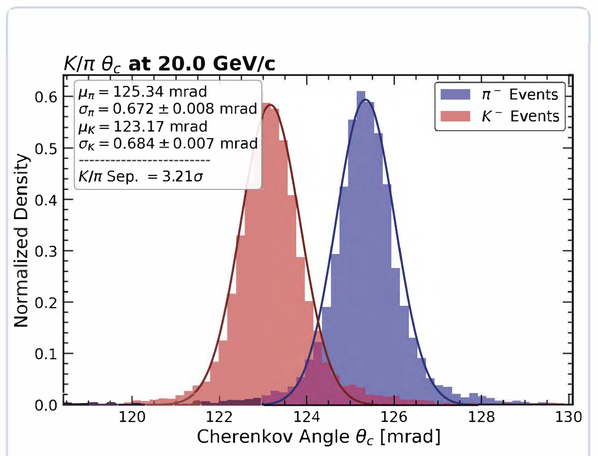


Fig. 13: Reconstructed θ_c at 20 GeV/c (θ = 15°, 3.21σ).

6. Reflection Reconstruction & Cylindrical Mirror Resolution Study

- **Geometric Unfolding ($E \to S \to M \to D$):** Solve virtual refraction point (x_S, y_S) from (x_E, y_E) and reflected hit (x_D, y_D) via geometric optics to reconstruct θ_c.
- **Degradation at θ = 25°:** Mean θ_c is unchanged (μ_π = 125.58 mrad), while σ_{θ_c} broadens from 0.67 to 0.80 mrad, reducing K/π separation from **3.21σ (θ = 15°)** to **2.65σ (θ = 25°)**.
- **Root Cause & Mitigation:** Cylindrical mirror (R = 56.3 cm) stretches a 1 × 1 mm^2 SiPM pixel into ~1.00 × 1.28 mm^2 tangentially (r/B = 1.28). **Planar mirrors** are proposed.

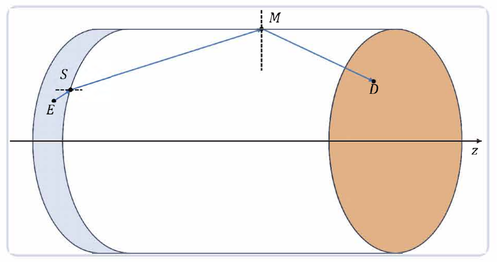


Fig. 14: Reflection unfolding geometry.

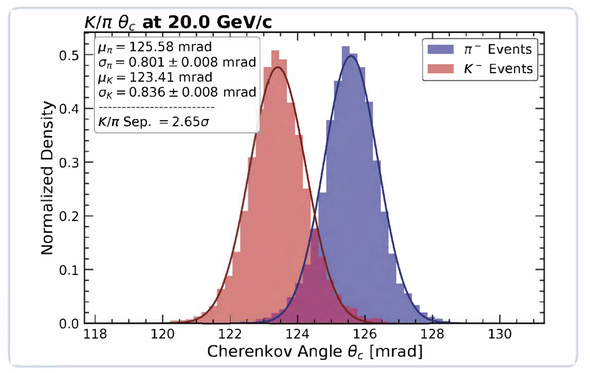


Fig. 15: Reflected ring θ_c (θ = 25°, 2.65σ).

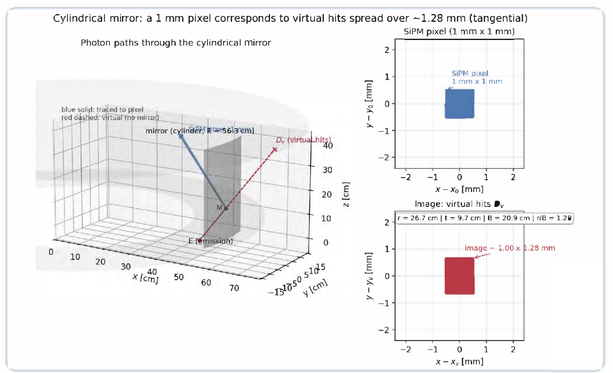


Fig. 16: Tangential virtual pixel stretch.

7. Dual-Radiator Upgrade Concept for 40 GeV/c K/π Separation

- **100 cm Dual-Radiator Architecture:** To extend **K/π separation up to 40 GeV/c**, an extended module (0.95 < $|\cos\theta|$ < 0.99, z ≈ 1500–2500 mm) combining a 6 cm 3-layer aerogel (n ≈ 1.03) and an L = 90 cm gas radiator is explored, forming concentric outer (aerogel) and inner (gas) Cherenkov rings.
- **Focusing Optimization:** Continuous photon emission along the 90 cm gas path introduces large σ_{emission}; optical focusing via mirrors/lenses to redirect photons onto the 2.5 mm detector plane is under active study.

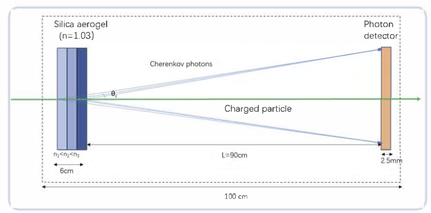


Fig. 17: Dual-radiator concept.

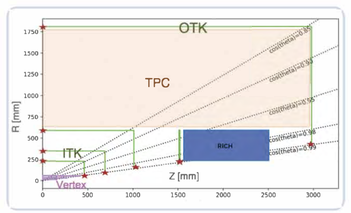


Fig. 18: Extended RICH location.

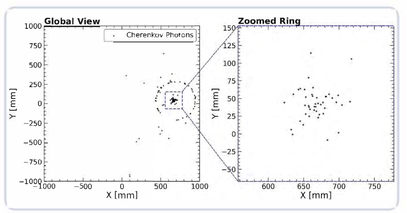


Fig. 19: Dual-radiator photon hit map.

8. Summary & Next Steps

Key Achievements:

- **Simulation Chain Established:** Full DD4hep + Geant4 optical transport & SiPM digitization in CEPCSW.
- **Focusing Aerogel Validated:** 3-layer gradient n suppresses σ_{emission}.
- **Benchmark Met:** 1 mm SiPM achieves **3.21σ K/π separation at 20 GeV/c** (θ = 15°).

Outlook & Next Steps:

- **01. Dark-Noise Impact:** Quantify PID degradation vs. dark count rate.
- **02. Advanced Reconstruction:** Maximum Likelihood + Hough Transform for noisy & reflected rings.
- **03. Full-Chain PID Evaluation:** Performance with realistic response & planar mirrors.

Presenter: Changru Li (UCAS / IHEP, CAS) | **Contact Email:** licr@ihep.ac.cn

C15

Silicon Photomultipliers for the CEPC Forward Aerogel RICH: Survey and Test System

Haojie Dong[1,2], Zhonghua Qin[2], Changru Li[2], Jian Wang[2], Qingmin Zhang[1]

[1] Xi'an Jiaotong University [2] Institute of High Energy Physics, CAS

CEPC 2026 International Workshop · Shanghai · October 2026

1 Introduction

- CEPC will produce unprecedented samples of Z and Higgs bosons; flavour physics benefits from identifying kaons among far more abundant pions [1].
- In the forward region, time of flight separates K/π only below **~3 GeV/c**, and TPC dN/dx degrades on shorter track paths [2].
- A proximity-focusing **aerogel RICH** (n ≈ 1.008) measures the Cherenkov angle, $\cos\theta_c = 1/(n\beta)$, targeting **3σ K/π up to 20 GeV/c** [3].
- A few tens of photons per track in 3 T: the sensor needs high PDE, mm pixels, low DCR and radiation tolerance — **SiPM is the baseline**.

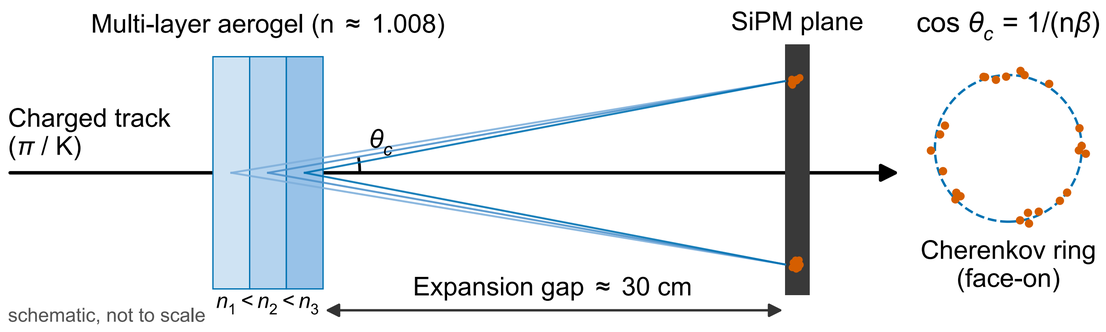


Fig. 1 Proximity-focusing multi-layer aerogel RICH (schematic): n rises layer by layer.

2 SiPM Survey

Requirements

Parameter	Requirement
Spectral range	> 300 nm
Peak PDE	~50 %
Pixel size	1 mm (or 3–6 mm with charge sharing)
Spatial resolution	~300 μm
Time resolution	100–200 ps
Dark count rate	100–200 kHz/mm² at room temperature
Crosstalk	1–5 %
Radiation tolerance	10^{12}–10^{13} n_{eq}/cm²
Total area	~1.6 m²

Preliminary specification [4]

Six vendors, 43 datasheets

Vendor	Peak PDE	Pixel	DCR (kHz/mm²)	Crosstalk	SPTR [12,13]
Hamamatsu (JP) [5]	48–50 %	1–6 mm	**41–167**	**3–10 %**	~117ps*
Broadcom (US) [6]	**63 %**	2–4 mm	111–270	9–34 %	~66 ps*
onsemi (US) [7]	41–50 %	1–6 mm	**30–150**	7–25 %	n.p.
NDL (CN) [8]	45–48 %	1–6 mm	150–650	n.p.	n.p.
Joinbon (CN) [9]	32–35 %	1–3 mm	88–288	3–3.5 %	n.p.
FBK (IT) [10,11]	**60–63 %**	1–2 mm	**~100**	15–20 %	**< 50 ps***

Typical room-temperature datasheet values; orange = favourable values; * literature or measurement; n.p. = not published; FBK devices are custom-made.

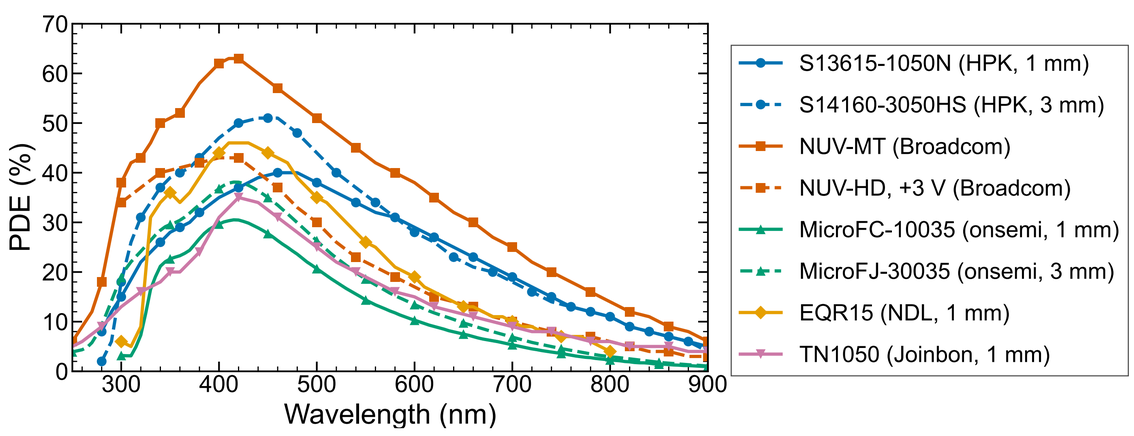


Fig. 2 PDE spectra of representative devices, digitized from vendor datasheets.

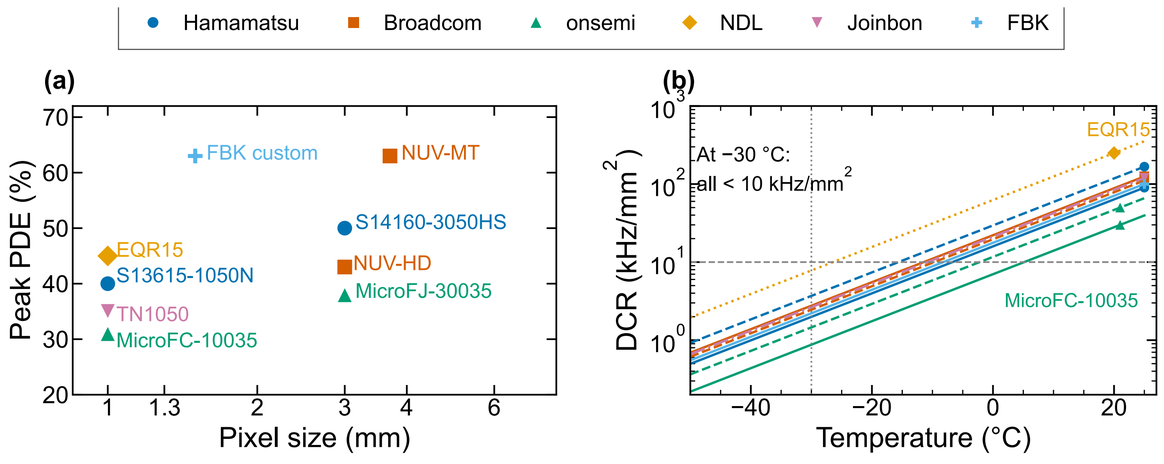


Fig. 3 (a) Peak PDE vs pixel size (b) Dark count rate vs temperature

Survey key findings

- Highest PDE: **Broadcom NUV-MT and FBK (60–63 % at 420 nm)**; lowest DCR: **onsemi (30 kHz/mm²)**.
- onsemi, NDL and Joinbon publish no timing data; **no vendor publishes radiation tolerance**.
- Cooling helps: DCR **halves every ~10 °C**; at −30 °C all devices in Fig. 3b are **below 10 kHz/mm²**.
- Irradiation hurts: DCR grows linearly with fluence [14–16], **so cooling is essential.**

Three candidate devices

Device	Pixel	PDE	DCR	Crosstalk	Why selected
Hamamatsu S14161-3050HS	3 mm	50 %	~167†	7 %	Best PDE–crosstalk balance; best-documented irradiation data
onsemi MicroFJ-30035	3 mm	38 %	50	8 %	Low DCR at low voltage; reference for cooling studies
NDL EQR15 11-1010D-S	1 mm	45 %	250	n.p.	Highest PDE among 1 mm devices; domestic supply

Datasheet values at room temperature and the vendor-recommended overvoltage (onsemi: +2.5 V). PDE at peak wavelength (450 nm for Hamamatsu, 420 nm otherwise); DCR in kHz/mm²; † estimated from dark current, not an official specification; n.p. = not published. S14161-3050HS is the TSV array of the S14160-3050HS chip shown in Figs. 2–3.

3 SiPM Test System at IHEP

- Readout: **CAEN A5202** [17] (64 ch, Citiroc-1A) controlled by Janus software over Ethernet.
- Sensor: **Hamamatsu S16088** from JUNO-TAO — 4 × 8 chips of 12 × 6 mm², paired into 16 channels of 12 × 12 mm².
- Light & cooling: pulsed LED with optical filter in a dark box; climate chamber at **~5 °C**.
- The large channel area (12 × 12 mm², two chips in parallel) brings high dark noise, which makes the photoelectron peaks less clear.

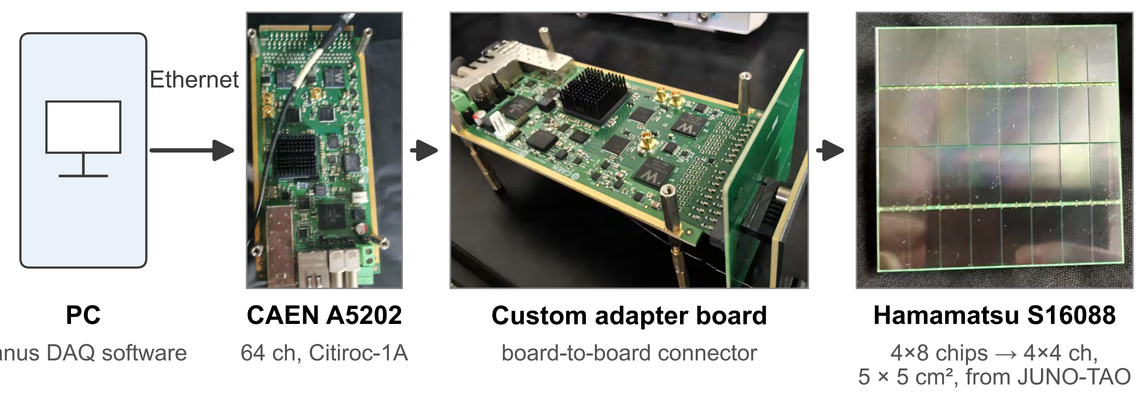


Fig. 4 Readout chain of the IHEP SiPM test system.

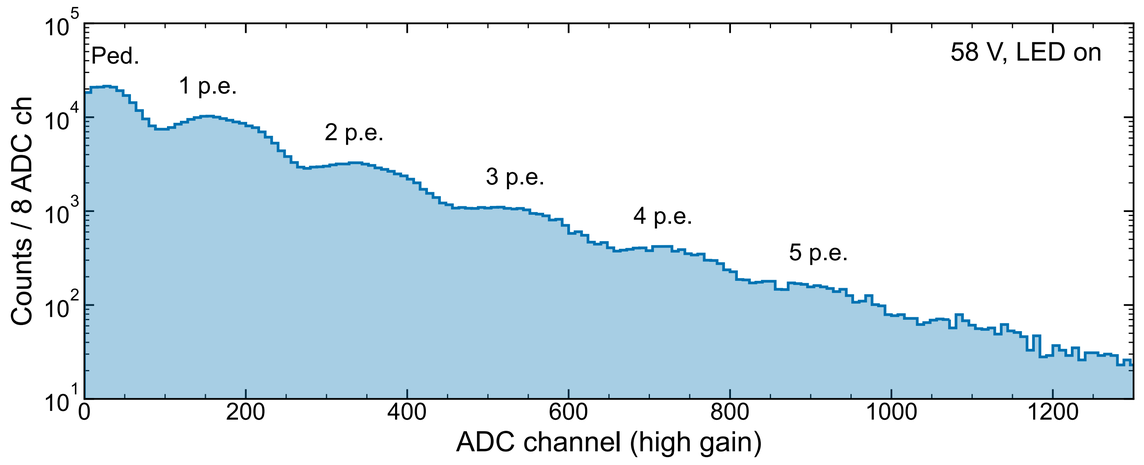


Fig. 5 LED charge spectrum of one S16088 channel at 58 V and ~5 °C: pedestal and 1–5 p.e. peaks are resolved.

4 Summary

- Six SiPM vendors compared against the forward-RICH requirements using **43 datasheets**; **three candidate devices** selected.
- Market gap: **no 1 mm pixel with PDE > 50 %**, and no published radiation tolerance.
- Irradiation-driven dark counts require operation at **−30 °C or below**.
- An SiPM test system is **running at IHEP**; S16088 LED spectra resolve **photoelectron peaks up to 5 p.e.**
- Next: colder operation, breakdown-voltage measurement, then gain, DCR, PDE and timing of candidate SiPMs.

References: [1] CEPC Study Group, CEPC Technical Design Report – Reference Detector, arXiv:2510.05260 (2025). [2] D. Yu, H. Ding et al., arXiv:2507.18164 (2025). [3] A.Yu. Barnyakov et al., arXiv:2604.08962 (2026). [4] Z. Qin, Investigation of an Endcap Cherenkov Detector for CEPC, Guangzhou, 15 July 2026. [5] Hamamatsu datasheets: S13615, S14160/S14161, S16088 (K30-I50549). [6] Broadcom datasheets: AFBR-S4N44P164M, AFBR-S4N22P014M (NUV-MT); NUV-HD. [7] onsemi datasheets: C-Series, J-Series. [8] NDL datasheets: EQR15, EQR20, PSS. [9] Joinbon datasheets: TN1000 and TN3000 Series, JARY-TN1050-8×8C. [10] A. Gola et al., Sensors 19 (2019) 308. [11] A. Gola, CERN Detector Seminar, 21 April 2023. [12] S. Gundacker et al., Phys. Med. Biol. 65 (2020) 025001. [13] S. Gundacker, SiPM single photon timing resolution, 2nd DRD4 Collaboration Meeting, CERN, 23 Oct. 2024. [14] E. Garutti, Yu. Musienko, Nucl. Instrum. Meth. A 926 (2019) 69. [15] S. Merzi et al., Sensors 24 (2024) 4990. [16] M. Calvi et al., Nucl. Instrum. Meth. A 922 (2019) 243. [17] CAEN, A5202/DT5202 User Manual, UM7945 (2023).